

1 **Computational evidence of a new allosteric communication**
2 **pathway between active sites and putative regulatory sites in the**
3 **alanine racemase of *Mycobacterium tuberculosis***

4 Short title: Dynamics of alanine racemases reveal new allosteric sites in *M. tb*

5 Alr

6 Jayanthi Jyothikumar^{##}, Sushil Chandani^{1*}, Tangirala Ramakrishna[#]

7 [#]Not affiliated currently

8 ¹New Biological Entities, Hyderabad, Telangana, India.

9 ^{*}Corresponding author

10 E-mail address: jayojir@gmail.com (JJ)

11 E-mail address: sushilchandani@gmail.com (SC)

12

13

14

15

16

17

18

19

20

21

22 **Abstract**

23 Alanine racemase, a popular drug target from *Mycobacterium tuberculosis*,
24 catalyzes the biosynthesis of D-alanine, an essential component in bacterial cell walls. With
25 the help of elastic network models of alanine racemase from *Mycobacterium tuberculosis*, we
26 show that the mycobacterial enzyme fluctuates between two undiscovered states—a closed
27 and an open state. A previous experimental screen identified several drug-like lead
28 compounds against the mycobacterial alanine racemase, whose inhibitory mechanisms are
29 not known. Docking simulations of the inhibitor leads onto the mycobacterial enzyme
30 conformations obtained from the dynamics of the enzyme provide first clues to a putative
31 regulatory role for two new pockets targeted by the leads. Further, our results implicate the
32 movements of a short helix, behind the communication between the new pockets and the
33 active site, indicating allosteric mechanisms for the inhibition. Based on our findings, we
34 theorize that catalysis is feasible only in the open state. The putative regulatory pockets and
35 the enzyme fluctuations are conserved across several alanine racemase homologs from
36 diverse bacterial species, mostly pathogenic, pointing to a common regulatory mechanism
37 important in drug discovery.

38 **Author summary**

39 In spite of the discovery of many inhibitors against the TB-causing pathogen
40 *Mycobacterium tuberculosis*, only a very few have reached the market as effective TB drugs.
41 Most of the marketed TB drugs induce toxic side effects in patients, as they non-specifically
42 target human cells in addition to pathogens. One such TB drug, D-cycloserine, targets
43 pyridoxal phosphate moiety non-specifically regardless of whether it is present in the
44 pathogen or the human host enzymes. D-cycloserine was developed to inactivate alanine
45 racemase in TB causing pathogen. Alanine racemase is a bacterial enzyme essential in cell

46 wall synthesis. Serious side effects caused by TB drugs like D-cycloserine, lead to patients'
47 non-compliance with treatment regimen, often causing fatal outcomes. Current drug
48 discovery efforts focus on finding specific, non-toxic TB drugs. Through computational
49 studies, we have identified new pockets on the mycobacterial alanine racemase and show that
50 they can bind drug-like compounds. The location of these pockets away from the pyridoxal
51 phosphate-containing active site, make them attractive target sites for novel, specific TB
52 drugs. We demonstrate the presence of these pockets in alanine racemases from several
53 pathogens and expect our findings to accelerate the discovery of non-toxic drugs against TB
54 and other bacterial infections.

55 **Introduction**

56 Tuberculosis is one of the top 10 causes of mortality globally and according
57 to latest available estimates, 10.4 million people developed this disease in 2016, of which 4.9
58 million people were infected with multidrug-resistant TB strains (MDR-TB) [1]. The
59 prevalence of multidrug-resistant TB (MDR-TB) and extensively drug-resistant tuberculosis
60 (XDR-TB) necessitates the inclusion of novel anti-tubercular therapies and strategies in the
61 treatment of TB. Treatment regimen comprising simultaneous use of multiple drugs is the
62 current strategy in practice [2]. Despite the implementation of this strategy, TB mortality
63 rates have not abated. Therefore, efforts to eradicate the TB pandemic have been stepped up
64 globally through research oriented towards finding new drugs against the tubercle bacilli [3].

65 Alanine racemase (EC 5.1.1.1; Alr), an essential bacterial enzyme [4] is a
66 popular drug target due to the absence of human homologs. The enzyme catalyzes the inter-
67 conversion of L- and D-alanine and requires pyridoxal 5'-phosphate (PLP) as a cofactor. PLP
68 is covalently attached to the enzyme through an internal Schiff's base linkage [5]. In the L to
69 D direction, the enzyme catalyzes the formation of D-alanine, an essential component of D-

70 alanyl-D-alanine found in the peptidoglycan layer in bacterial cell walls [5]. In some bacteria
71 including *Escherichia coli* [6], *Salmonella typhimurium* [7] and *Pseudomonas aeruginosa*
72 [8], there are two Alr isozymes (Alr1 and Alr2 (aka DadX)), responsible for the anabolic and
73 catabolic functions respectively.

74 The catalytically active form of Alr is a dimer [9], due to the participation of
75 residues from both the monomers towards the formation of a functional active site. A narrow
76 passage from the exterior forms an entryway to the substrate binding cavity in the active site
77 and is lined by conserved residues, some of which have been demonstrated to orient the
78 substrate molecules during their entry into the active site [10, 11]. In Alr_{Mtb}, the substrate
79 binding cavity is a small, conical space gated by two tyrosine residues (inner gates), which
80 restrict the entry of substances into the active site [12]. Carboxylates such as acetate,
81 propionate and substrate analogs such as alanine phosphonate co-crystallize in the substrate
82 binding cavities of alanine racemases [13–15] and are suggested to regulate catalysis by
83 competitive inhibition, though the exact control mechanisms are not known [16].

84 Including the structure of Alr_{Mtb} [12], there are around a dozen and a half
85 unique alanine racemase structures in protein databases [13, 17–23]. Though there has been
86 considerable interest in elucidating the detailed catalytic mechanism of D- to L-alanine
87 racemization in several organisms [5, 10, 24, 25], the regulatory aspects of catalysis suffer
88 from lack of research. In spite of the discovery of a plethora of inhibitors against pathogenic
89 Alr [26–28], only one of them has reached the market as a TB drug. This drug (D-
90 cycloserine) is a structural analog of D-alanine and binds to all PLP-containing enzymes non-
91 specifically, including those in the host, inducing toxic side-effects [29]. Current drug
92 discovery efforts focus on finding safer, selective, non-substrate inhibitors. Several inhibitors
93 of Alr are non-substrate leads, whose target sites on the enzyme are not known. Of these, five
94 were shown to be non-toxic to mammalian cells in a high-throughput screen for anti-

95 tubercular small molecule inhibitors [28]. Until now, there have been no studies concerning
96 the binding sites of these five drug-like leads (Fig 1) on the enzyme. Considering the
97 numerous hurdles in culturing *M. tb* and the urgency in developing novel drugs to contain the
98 superbug strains, we sought to determine the target sites of these leads through computational
99 studies.

Fig 1 Inhibitors shortlisted from Anthony et al., 2011 [28]. IUPAC names and molecular weights are shown for each lead inhibitor. All of the listed inhibitors obey Lipinski's 'rule of 5' characteristic of drug-like compounds and were shown to be non-cytotoxic to mammalian cells [28].

100 In recent years, normal mode analysis (NMA) has been widely used in
101 probing large-scale, collective motions of proteins and has been increasingly utilized to
102 characterize the dynamic aspects of enzymes [30–32]. Particularly, elastic network model
103 (ENM) based NMA has been useful in studying intrinsic dynamics of slow protein motions
104 over longer timescales [33, 34]. Computationally, the generation of elastic network models of
105 diverse protein conformations is less expensive compared to molecular dynamics (MD)
106 simulations [35]. In enzymes, ENM-NMA-predicted global motions represent biologically
107 relevant functional motions and have been shown to include local fluctuations such as loop
108 movements essential in catalysis [36]. We searched ENM-based Alr_{Mtb} conformations for
109 target sites of lead inhibitors through multiple, robust search algorithms by a blind docking
110 strategy (BD). BD remains a common choice in the discovery of novel, allosteric binding
111 sites [37, 38]. In conjunction with pocket search tools, BD is capable of identifying new
112 functional pockets on the target protein [39]. This strategy helped us in the successful
113 identification and validation of new pockets in Alr_{Mtb}. Further to the above investigations, a
114 comparative study of the intrinsic dynamics of Alr homologs with the help of a range of
115 computational tools helped us gain new insights into the regulatory aspect of D-alanine
116 synthesis.

117 **Results / Discussion**

118 **All-atom normal mode analysis**

119 **The putative regulatory pockets are conserved across homologs** The crystal structure of

120 Alr_{Mtb} is a kidney-shaped dimer, with two active site cavities opening on the convex side

121 (Figs 2A, 2C and 2E) and two pockets located on the concave side (Figs 2A and 2D).

122 Residues found to be missing (Fig 2B) in the crystal structure were from both internal and

123 terminal regions. The internal stretches of missing residues (176–180 of subunit A and 266–

124 280 of subunit B), pertained to the same region, i.e., the mouth region of the first active site

125 cavity (Fig 2E).

Fig 2 Structure of alanine racemase from *Mycobacterium tuberculosis*. A. Molecular surface representation of the structure of alanine racemase (monomers A and B shown in green and cyan colours respectively). Magnified region shows the putative dimer interface groove (DIG) pocket on the dimer interface. B. Unresolved regions in the crystal structure of Alr indicated by different colours in the cartoon representation of the enzyme (missing N-terminus—yellow; missing C-terminus—blue; missing internal stretches—red). C. TIM-barrel of active site 2 showing the cofactor PLP (red sticks) covalently attached to the catalytic residue Lys44 (green sticks). Note that the active site is composed of residues from both monomers (B monomer shown in cyan colour and residues from A monomer are coloured green) D. Surface representation of the enzyme showing the putative regulatory sites (yellow) E. Surface representation of the enzyme showing tiny pockets (pink) flanked on either side by the active site cavities (red). (Due to the revision in UniProt sequence information, the residue numbers given in this work should be decremented by 2 in order to compare with the numbering provided in LeMagueres et al., 2005 [12]. For example, the residues, 176–180 in our work refer to residues, 174–178 in LeMagueres et al., 2005 [12]).

126 Alignment of the protein sequences of Alr homologs (Figs 3, S1 and S2)

127 revealed highly similar residues in the newly identified regions (described later): dimer

128 interface groove region (Fig 3B), putative regulatory sites (Fig 3C) and a short helix (Fig

129 3D). On the other hand, the N-termini of the homologous Alr were of different lengths and

130 were dissimilar in sequence composition (Fig 3A). Despite the presence of terminus in their

131 sequences, 8 of the crystal structures of the homologs were devoid of either the N-terminus

132 (varied between 3–15 residues) or the C-terminus (varied between 1–6 residues) or both. Of

133 the remaining structures, eight were complete and showed disordered coils in their termini.
134 Both PSI-PRED (secondary structure predictor based on position-specific-scoring-matrices of
135 unique fold libraries) and Phyre2 (protein structure modeller based on a combination of *ab*
136 *initio* and template-based strategies) generated highly disordered coils in the terminal regions
137 (1–12 and 384–386) of *M. tb* racemase. Compared to the rest of the protein, the average B-
138 factor values in the termini of most of the alanine racemases displayed a marginal increase.
139 However, *Streptomyces lavendulae* (PDB ids: 1VFH, 1VFT, 1VFS), the closest structural
140 homolog of Alr_{Mtb} (49% sequence identity), displayed 2–3 times higher values in the N-
141 terminal regions signifying a mobile terminus.

Fig 3 Structure-based multiple sequence alignment of alanine racemases. A. Aligned N-terminal region lacking definite secondary structures. B. Aligned DIG (dimer interface groove) pocket region. C. Aligned putative regulatory pocket and tiny pocket regions. D. Aligned region of the short helix (H2) residues implicated in the allosteric communication between the putative regulatory pockets and the active site residues. Shaded circles in different colours beneath the alignment show the residues in the corresponding pockets. (The alignment included sequences of *M. tuberculosis* (PDB code: 1XFC), *S. lavendulae* (PDB code: 1VFH), *S. coelicolor* (PDB code: 5FAC), *C. glutamicum* (PDB code: 2DY3), *B. subtilis* (PDB code: 5IRP), *C. difficile* 630 (PDB code: 4LUT), *B. anthracis* (Ames) (PDB code: 2VD9), *S. aureus* (PDB code: 3OO2), *E. faecalis* (PDB code: 3E5P), *C. subterraneus subsp. tengcongensis* (PDB code: 4Y2W), *E. coli* (PDB code: 2RJG), *S. pneumoniae* (PDB code: 3S46), *P. fluorescens* (PDB code: 2ODO), *P. aeruginosa* (PDB code: 1RCQ), *A. baumannii* (PDB code: 4QHR), *B. henselae* (PDB code: 3KW3). X denotes cofactor ‘PLP-Lysine’ adduct, also called LLP).

142 Pockets were searched for in Alr_{Mtb} as described in Methods after modeling
143 the missing residues into its crystal structure. Pocket analysis of the Alr_{Mtb} dimer model
144 revealed the presence of two surface pockets beneath the terminal disordered coils. The
145 pockets were adjacent to each other at the dimer interface, one corresponding to each subunit
146 (Fig 2D). An examination of the crystal structures of the homologs revealed the existence of
147 such pockets, either exposed to the exterior (PDB ids: 2RJG, 3E5P, 1RCQ, 2ODO) or
148 sequestered beneath the terminal regions (PDB ids: 3S46, 2VD9, 4Y2W). Closed pockets
149 sequestered beneath the termini were spacious enough to accommodate typical drug-like

150 small molecules (combined Connolly's molecular surface volumes of the two pockets were
151 358 \AA^3 , 900.4 \AA^3 , 834 \AA^3 in 3S46, 2VD9, 4Y2W respectively). The inadvertent inclusion of
152 extra diagonal spaces in the pocket volume calculations of Alr_{Mtb} and the longer, lid-like N-
153 termini (Fig 3A) resulted in a single larger pocket in *M. tuberculosis* (combined Connolly's
154 molecular surface volume of the two pockets in the closed state of Alr_{Mtb} = 4355.9 \AA^3). In the
155 current discussion, the mere presence of these pockets across species is of significance.
156 Across homologs, two blocks of pocket residues (Fig 3C) were found to be conserved: region
157 292–295 in Alr_{Mtb} (part of a conserved motif GY[AG]DG) and region 370–375 in Alr_{Mtb} (375
158 is completely conserved, 372 is partially conserved). These regions were not exposed to the
159 solvent in the crystal structures with sequestered pockets.

160 Upon examination of the normal modes of Alr_{Mtb}, we observed that two low-
161 frequency normal modes, LF₈ and LF₁₀ displayed the gradual closure of N-terminal regions
162 over the surface pockets. Of the 30 conformations of LF₈ (normal mode 8), 15 were non-
163 identical and described the enzyme transition between an open state (conformations 8 and 9)
164 and a closed state (conformations 23 and 24). The spectrum of conformations between the 9th
165 and 23rd showed the surface pockets at various stages of closure. Fluctuation plot of the
166 normal mode 8 (Figs 4A and 4B) revealed that the close-open movements of the terminal
167 regions are events, resulting from the closing and opening of the bulky N-terminal domains
168 of the enzyme. In other words, the terminal regions always moved along with the other
169 fluctuating regions in the mode 8 enzyme conformations. Such large-scale movements
170 involving entire domains were observed in every examined homolog (shown as cumulative
171 root mean square displacement (cRMS) plots in Figs 4C–4H). In the cRMS plots, fluctuation
172 patterns of Alr were extremely similar in the bacterial genera belonging to the same phylum
173 (Fig S3), viz., Actinobacteria (*M. tb* and *S. lavendulae*), Proteobacteria (*P.aeruginosa* and
174 *P.fluorescens*) and Firmicutes (*Streptococcus pneumoniae* and *Enterococcus faecalis*).

175 Overall, the fluctuation patterns, including the closure of the surface pockets (Movie S1)
176 occurring as part of N-terminal domain movements were similar in all of the examined Alr
177 homologs. In some of the homologs, the putative lid regions were shorter than those in *M. tb*.
178 In the closed conformations of such homologs, the pockets were not completely covered.

Fig 4 Fluctuations of bacterial alanine racemases. A. Putty cartoon view of fluctuations of Alr_{Mtb} (Graph in panel B) mapped onto residues of the mycobacterial Alr structure colored from low to high values (0–13 Å as yellow to red). B–H. Plots of atomic displacements (derived from all-atom normal mode analyses calculated on NOMAD-Ref server) of bacterial alanine racemases, *M. tuberculosis* (PDB code: 1XFC), *S. lavendulae* (PDB code: 1VFH), *E. faecalis* (PDB code: 3E5P), *S. pneumoniae* (PDB code: 3S46), *E. coli* (PDB code: 2RJG), *P. aeruginosa* (PDB code: 1RCQ), *P. fluorescens* (PDB code: 2ODO), respectively along normal mode number 8 (LF₈). Collectivity measures and frequencies of normal mode are indicated for each organism.

179 Additionally, when the fluctuations of the first 10 normal modes were
180 clustered (ensemble NMA based on C- α coordinates), higher amplitudes were observed in the
181 termini of the homologs, *Streptomyces lavendulae* and *Caldanaerobacter subterraneus*
182 *subsp. tengcongensis* (Fig 5). The conformational location of the terminus could be
183 responsible for the observed oscillations, but that does not appear to be the case due to the
184 following points:

- 185 1. Absence of definite secondary structures like α -helix or β -strand in the terminal
186 regions of the structures of homologs.
- 187 2. Location of the disordered, flexible terminal regions over surface pockets in Alr
188 homologs.
- 189 3. Presence of the pockets in one of the states in the crystal structures of homologs:
190 ‘sequestered’ or ‘exposed’.
- 191 4. Closing and opening of the pockets during the intrinsic movements of the enzyme in
192 normal mode simulations.
- 193 5. Docking of lead inhibitors to the surface pockets (discussed later).

194 Therefore, we conclude that the terminal fragments (especially the longer N-
195 terminal 1–12 residue region in *M. tb*) anchored over the surface pockets help in sequestering
196 small molecules, which are bound to the pockets. We propose that the two pockets in
197 question are putative regulatory sites and refer to them as RS pockets (‘Regulatory Site’
198 pockets) throughout this study. As mentioned earlier, a few other regions in *Alr_{Mtb}* fluctuated
199 simultaneously with the close-open movements of the RS pockets:

- 200 1. Two new pockets (Fig 2A-magnified region) lying in the dimer interface junctions of
201 the enzyme were found to elongate and contract with concomitant increase and
202 decrease in their volumes. We name the pockets as DIG-A (Dimer Interface Groove
203 pocket of monomer A) and DIG-B (Dimer Interface Groove pocket of monomer B).
- 204 2. Two tiny pockets lying adjacent to each other, in-between the entrances of the active
205 site cavities (Fig 2E) exhibited close-open movements across the LF₈ ensemble of
206 conformations. The tiny pockets were high affinity binding sites of the native
207 substrate (alanine) in both the crystal structure and the ensemble conformations.
208 Charged residues, Arg373 and Glu367 of the tiny pockets were found to interact with
209 the substrate. Across the ensemble conformations, the tiny pockets remained closed
210 when the RS pockets were open. The tiny pockets and the RS pockets open on the
211 opposite faces of the enzyme and share a few residues (292, 373) between each other.
212 Other residues of the two pockets exhibit a unique arrangement in the sequence and
213 are placed side by side in an alternating fashion (Fig 3C). Consequently, the adjacent
214 residues in the structure belong to one of the two pockets and assume opposing states
215 at any given instant during the dynamics. Therefore, the tiny and the RS pockets may
216 be fulfilling opposing roles in regulation.

Fig 5 Cross species normal mode analysis of Alr. Ensemble normal mode analysis (eNMA) derived fluctuations (based on C- α coordinates) of the superimposed structures of the

homologs. Superimposition was based on a multiple sequence alignment of protein sequences of Alr homologs on Bio3D modules, which was then manually edited for errors (Text S1). The fluctuation profiles of the Alr homologs are stacked at off-set values of 0.5 between each other on the y-axis for clarity. Gaps in the graphs correspond to the gaps in the aligned sequences.

217 **N-terminal domain movements lead to closure of regulatory pockets** Normal modes of
218 frequencies less than 30 cm^{-1} , cover most of the amplitudes in atomic displacements [40, 41].
219 A previous study has shown that a single normal mode is capable of carrying a lot of
220 information on the conformational change of a given protein in terms of direction and pattern
221 of atomic displacements [42]. In Alr_{Mtb} , LF_8 adequately described movements between two
222 distinct states—one in which the putative RS pockets were open (Figs 6A, 6C) and the other
223 in which they were closed (Figs 6B, 6D). Nearly 67% of amino acid residues were found to
224 exhibit fluctuations (collectivity measure=0.6662). Among the all-atom normal mode
225 ensemble of 30 conformations defining LF_8 , the closed and open conformations were both
226 found twice each (conformations 8 and 9 represented open states while conformations 23 and
227 24 showed closed states). The pockets started closing from conformation 20 onwards and
228 were fully closed in conformations 23 and 24. In the 23rd and 24th closed conformations,
229 active site cavities were twisted from their original positions (Movie S1). A closer
230 examination of Alr_{Mtb} fluctuations showed that a twisted, hinge-like bending motion of the N-
231 terminal domains of each monomer, transformed the open state into the closed state (Fig 6).
232 The rigid body twist of the enzyme along the bulky N-terminal domains resulted in the
233 closure of the putative N-terminal lid region over the RS pockets. The closed and open state
234 fluctuations resembled the closing and opening of a door hinge with the two plates being the
235 N-terminal domains and the centre of the hinge being the far end of the C-terminal region.
236 Concordantly, higher deformation energies were seen in the pivot residues (96, 141, 146, 261
237 and 263) of the dimer interface pocket region (DIG pocket region), part of which is the far C-
238 terminal region (Fig 7). Apart from this hinge-like region, the putative terminal lid regions,

239 the catalytic tyrosine and the short helix region showed higher deformation energy peaks
240 signifying greater local flexibility (Fig 7).

241 **Fig 6 Depiction of transition of LF_s from an open to a closed conformation in Alr_{Mtb}.** (A)
242 and (B). Representation of the molecular surfaces of the open and closed states of the
243 mycobacterial alanine racemase. (C) and (D). Cartoon representations of the secondary
244 structures of open and closed states of Alr_{Mtb}. It can be noted that, the positions of helices (H3
245 and H4) have changed and the N-terminal putative lid-like regions are closed over the
246 regulatory pockets in the closed state.

Fig 7. Visualization of mycobacterial Alr structure on the basis of local flexibility. A plot
of residue-wise cumulative deformation energies derived from the first 10 low frequency
normal modes of mycobacterial alanine racemase (energies calculated on C- α NMA of Alr_{Mtb}
on a standalone implementation of Bio-3D package). The putty view of deformation energies
mapped onto mycobacterial Alr structure is coloured from low to high values (2–421 kcal /
mol as yellow to red).

247 Table 1 portrays the loss of the relative orientation of the active site residues
248 in space in the closed and open states as compared to that in the dimer model constructed
249 from the crystal structure of Alr_{Mtb} (See Methods). In the closed state of the active site 1, one
250 of the inner gates, Tyr273, was 2.4 Å nearer to the other inner gate tyrosine, Tyr366,
251 compared to their positions in the open state. As stated before, these two tyrosines guard the
252 entrance of the substrate binding cavity. As discussed in LeMagueres et al. [12], these two
253 residues define an opening of 2.7 Å in the crystal structure and are suggested by LeMagueres
254 et al. [12] to move apart in order to permit entry and exit of small molecules in and out of the
255 active site cavity. The distance between the two inner gates in the dimer model of crystal
256 structure was 13.7 Å. This value is intermediate to the distance between the inner gates in the
257 closed state (13.0 Å) and the distance between the same residues in the open state (15.4 Å).
258 Thus, in the open state, the gates have moved further apart by 1.7 Å when compared to the
259 distance between them in the model of the crystal structure. At the same time, the inner gates
260 have come closer by 0.7 Å and are essentially closed in the closed state. Therefore, the active
261 site entrance is closed in the closed state. The above results provide a proof for the hypothesis
262 put forth by LeMagueres et al. that the inner gates must move apart prior to catalysis [12].

Table 1 Distances between C- α atoms of the substrate binding cavity residues^a

Residue range	Active site 1				Active site 2			
	Distance between residues (Å)			Difference between open and closed states (Å)	Distance between residues (Å)			Difference between open and closed states (Å)
	Open state (Conf. 8 and 9)	Closed state (Conf. 23 and 24)	Dimer model (Model of crystal structure with missing residues) (Conf. 16)		Open state (Conf. 8 and 9)	Closed state (Conf. 23 and 24)	Dimer model (Model of crystal structure with missing residues) (Conf. 16)	
Tyr273 to Tyr 366 (Inner gates)	15.4	13.0	13.7	2.4	14.8	12.6	13.3	2.2
Tyr273 to Tyr48	19.3	18.4	18.1	0.9	18.7	18.1	17.6	0.6
Tyr273 to Met321	12.2	11.4	11.3	0.8	11.5	10.9	10.7	0.6
LYS44 to Tyr48	6.1	6.7	6.3	0.6	6.0	6.6	6.2	0.6
Tyr273 to Lys44	18.7	18.7	17.8	0	18.1	18.2	17.2	0.1
Cys320 to Tyr 366	10.0	9.5	9.5	0.5	10.1	9.6	9.6	0.5
Met321 to Tyr 366	8.1	7.7	7.7	0.4	8.0	7.7	7.7	0.3
Cys320 to Tyr48	12.6	12.9	12.4	0.3	12.7	13.1	12.5	0.4
Met321 to Lys44	9.5	9.2	9.0	0.3	9.5	9.3	9.0	0.2
Lys44 to Cys320	12.5	12.7	12.1	0.2	12.5	12.8	12.2	0.3
Tyr273 to Cys320	8.6	8.3	8.0	0.3	8.0	7.9	7.5	0.1
Met321 to Tyr48	9.1	9.3	8.9	0.2	9.2	9.4	8.9	0.2
Lys44 to Tyr 366	12.0	11.9	11.6	0.1	11.9	11.9	11.6	0
Tyr366 to Tyr48	7.4	7.5	7.2	0	7.4	7.5	7.2	0
Arg142 to Met321	14.2	13.7	13.5	0.5	13.8	13.3	13.1	0.5
Arg142 to Tyr366	21.0	19.4	19.6	1.6	20.7	19.2	19.4	1.5
Arg142 to Tyr273	10.4	10.0	9.6	0.4	10.4	10.2	9.7	0.2
Arg142 to Lys44	18.2	19.2	17.8	1.0	17.8	18.8	17.4	1.0
Arg142 to Tyr48	21.6	22.1	21.1	0.5	21.2	21.7	20.7	0.5

^acalculated on PyMOL molecular graphics tool

263 **Ensemble NMA (eNMA) uncovers conservation of conformational dynamics across**

264 **homologs**

265 Comparative ensemble NMA (eNMA) results showed that flexibility
266 profiles were largely similar across anabolic alanine racemases (PDB ids: 1XFC/*M. tb*;
267 1VFH/*Streptomyces lavendulae*; 2RJG/*Escherichia coli*; 3E5P/*Enterococcus faecalis*;
268 4Y2W/*Caldanaerobacter subterraneus subsp. tengcongensis*; 3S46/*Streptococcus*
269 *pneumoniae*) as well as their catabolic counterparts (1RCQ/*Pseudomonas aeruginosa*;
270 2ODO/*Pseudomonas fluorescens*) (Fig 5). Regions differing in amplitudes between the two
271 types of racemases included alignment position 40 (higher amplitude in anabolic racemases)
272 and alignment position 65 (higher amplitude in catabolic racemases). For the complete
273 multiple sequence alignment and the alignment positions utilized in ensemble NMA of
274 homologs, refer to Text S1. Across the homologs, the conserved residues constituting the
275 invariant core of the enzyme were found clustered around the same amplitude (Fig S4-A).
276 Moreover, the alignment positions displaying partial conservation of residues also fluctuated
277 more or less to the same extent (Fig S4-B). Notably, conserved residue positions of the active
278 site residues (alignment positions 51, 281 and 329 corresponding to Alr_{Mtb} residues 48, 273
279 and 321 resp.), putative RS pockets (alignment positions 77, 302 and 383 corresponding to
280 Alr_{Mtb} residues, 74, 294 and 375 resp.), DIG region (alignment position 149 corresponding to
281 Alr_{Mtb} residue, 144), ‘Second cavity opposite to PLP’ (refer to subsection 2 of section 3 for
282 details about this cavity) (alignment positions 140, 147, 179 and 330 corresponding to Alr_{Mtb}
283 residues 135, 142, 174 and 322) displayed nearly identical amplitudes across homologs.

284 In order to understand the nature of fluctuations between different regions of
285 the enzyme, we calculated dynamic cross-correlation maps (DCCM) of positional
286 fluctuations of amino acid residues (Fig 8). DCCM was based on the C- α coordinates of the
287 first 10 normal modes of Alr_{Mtb} as against the all-atom NMA results (discussed in the

288 previous sections). Figs 8A–8C show that the correlations between residue pairs in Alr_{Mtb} are
289 in excellent agreement with the all-atom NMA results (Figs 4A and 4B). Additionally,
290 DCCM provided insights into the directions of the movements between different regions. On
291 the whole, the region between residues 134 and 199, moved in opposite directions with
292 respect to the two flanking regions, 1–133 and 200–386. Both the completely correlated (Fig
293 8B) and completely anti-correlated (Fig 8C) regions revealed coupled networks of residues
294 that play a role in the close-open transition of the enzyme. For example, strong correlations
295 were seen in the following regions: putative lid region, catalytic lysine, RS pockets, tiny
296 pockets and the delimiting boundary residues of the substrate binding cavity. Similarly,
297 strong anti-correlations were seen between DIG residues (143, 144, 146 and 149), and the
298 regions listed in Table 2. Majority of the residues of the ‘Second cavity opposite to PLP’
299 moved in opposite directions with respect to all the other regions of the enzyme. In agreement
300 with the all-atom normal mode results, the inner gates of the substrate binding cavity moved
301 with equal amplitudes in opposite directions. Thus, inner gates were moving away from each
302 other during the transition of the closed state to the open state. Noticeably, the movement of
303 the inner gates was occurring as a result of the movement and expansion of the entire active
304 site. Thus the DCCM of Alr_{Mtb} derived from C- α fluctuations forms an additional proof for
305 the conclusion derived earlier from the all-atom NMA of Alr_{Mtb} that the inner gates must
306 move prior to catalysis.

Fig 8. Correlation map revealing correlated and anti-correlated regions in Alr. A. Heatmap showing the dynamic cross correlation map of C- α atom fluctuations derived from an NMA of the first 10 low frequency modes of mycobacterial alanine racemase. Red regions denote the completely correlated residue pairs (same period, same phase) while blue regions denote the completely anti-correlated residue pairs (same period, opposite phase). White regions correspond to residue pairs whose fluctuations are not correlated. The top and right multi-colour bars on the heatmap correspond to various enzyme regions (coloured for easy visualization). B. Strongly correlated motions between mycobacterial Alr residues. Red lines portray the strong correlations between the regions mapped on the representative circle of a mycobacterial Alr monomer. C. Strongly anti-correlated motions between mycobacterial Alr residues. Blue lines portray the strong anti-correlations between the regions mapped on the

representative circle of a mycobacterial Alr monomer. D. Dynamic cross correlation map of residual fluctuations derived from an ensemble-NMA of the first 10 low frequency modes of alanine racemases from 8 different bacterial species. Only those correlations present in all the 8 structures are shown in the plot.

Table 2 List of newly discovered target sites and their putative interactions with the inhibitors

No.	Enzyme pocket	Ligand	Docking tools finding the enzyme-ligand complex	Enzyme residues involved in non-covalent interactions
1	Putative RS pocket	L2-05, L2-06	Vina, SwissDock	Ala45, Asp46, Glu74, Ala293, Gly374, Arg375, Arg378
		L2-10, L2-13	Vina, SwissDock, PatchDock	
2	DIG pocket region	L2-05, L2-06, L2-10	Vina, PatchDock, SwissDock	Asp137, Gly139, Asn141, Gly146, Gln149, Arg192, Gln199, Lys263, Arg266, Glu269, Gly270
		L2-13	Vina, SwissDock	
3	Tiny pocket	Alanine	Vina	Tyr292, Gly295, Ser299, Glu367, Ser371, Arg373
4	Second cavity opposite to PLP (cavity characterized in a previous study [12])	L2-05, L2-06, L2-10, L2-13	Vina, PatchDock	Trp90, Lys135, Arg142, His174, Asp322, Gln323

307 Both the correlation networks (Figs 8B and 8C) are each made of complete
 308 graphs with well-connected nodes. The highly connected nodes in both the networks are hub-
 309 like ‘hotspots’ which moved together either in the same or different directions. Therefore,
 310 perturbing any of the sites corresponding to these hotspot nodes, by targeting them with small
 311 molecules, would affect the regulatory control of catalysis, as all of these sites are involved in
 312 the transition of the enzyme from an open to a closed state.

313 In order to understand the pattern of correlations across homologs, we
 314 compared a residual fluctuation map showing only those correlations present in all the eight
 315 homologs (Fig 8D) with the individual DCCM of each homolog (Figs 8A, S5–S11). We
 316 found that the correlated and anti-correlated regions were nearly the same in all the maps,

317 pointing to an evolutionary conservation of dynamics across alanine racemases. This
 318 conclusion is reiterated by the results of a comparative assessment of the normal modes of
 319 pairs of homologs using similarity measures of dynamics including RMSIP (Root Mean
 320 Square Inner Product) and Bhattacharyya coefficient (BC) (Table 3). RMSIP measures the
 321 similarity of atomic fluctuations derived from normal modes between proteins, whereas BC
 322 compares the covariance matrices obtained from the normal modes as elaborated in the
 323 Methods section. For example, a thermo-stable Alr from *Caldanaerobacter subterraneus*
 324 *subsp. tengcongensis*, which is a remote homolog of Alr_{Mtb} (sequence identity=28.6%) shows
 325 99.84% similarity in dynamics, as measured by the Bhattacharyya coefficient. Though the
 326 differences between the RMSIP scores were more pronounced than those of BC (Table 3),
 327 the latter is generally considered to be a better index for assessing the similarity of dynamics,
 328 as it incorporates eigenvalues. It is to be noted that RMSIP does not represent the energetic
 329 separation between the modes in the sets [43]. Sequence and structural similarity measures
 330 such as RMSD values scored lesser than dynamics similarity measures such as RMSIP and
 331 BC values (Table 3), proving that the conservation of dynamics far exceeds the sequence and
 332 structural conservation in alanine racemases.

Table 3 Measures of sequence, structural and dynamic similarity of alanine racemases across bacteria.

Alr homologs compared		Structural similarity (RMSD in Å)	% Sequence identity	% Sequence similarity	% Dynamic similarity ^{ab}	
					RMSIP	BC
<i>M. tb</i>	<i>S. lavendulae</i>	1.86	46.7	61.8	84.09	93.8072
<i>M. tb</i>	<i>E. coli</i>	2.496	34.2	48.7	90.54	99.8376
<i>M. tb</i>	<i>E. faecalis</i>	2.168	34.0	47.1	92.11	99.8416
<i>M. tb</i>	<i>S. pneumoniae</i>	2.515	33.5	50.4	89.66	99.7842
<i>M. tb</i>	<i>C. subterraneus</i>	2.056	28.6	46.9	94.27	99.8444
<i>M. tb</i>	<i>P. aeruginosa</i>	2.531	34	47.6	90.02	99.8891
<i>M. tb</i>	<i>P.fluorescens</i>	2.471	34.4	48.7	90.83	99.9071
<i>S. lavendulae</i>	<i>E. coli</i>	2.223	36.1	49.2	85.08	94.5419
<i>S. lavendulae</i>	<i>E. faecalis</i>	2.298	34	50	83.66	92.3979
<i>S. lavendulae</i>	<i>S. pneumoniae</i>	2.363	37.2	52.7	84.65	93.6492

<i>S. lavendulae</i>	<i>C. subterraneus</i>	2.161	33.1	52.3	83.69	92.8465
<i>S. lavendulae</i>	<i>P. aeruginosa</i>	2.391	37.9	50	82.69	90.3598
<i>S. lavendulae</i>	<i>P. fluorescens</i>	2.338	37.1	47.2	84.61	92.6982
<i>E. coli</i>	<i>E. faecalis</i>	2.371	31.5	48.4	93.07	99.8565
<i>E. coli</i>	<i>S. pneumoniae</i>	2.512	30.9	50	93.85	99.929
<i>E. coli</i>	<i>C. subterraneus</i>	2.759	28.7	47.1	91.23	99.6967
<i>E. coli</i>	<i>P. aeruginosa</i>	1.658	46.8	62	94.74	99.9699
<i>E. coli</i>	<i>P. fluorescens</i>	1.65	46.3	62.6	96.38	99.9606
<i>E. faecalis</i>	<i>S. pneumoniae</i>	1.608	52.3	65.2	94.79	99.929
<i>E. faecalis</i>	<i>C. subterraneus</i>	2.123	33.9	56.7	94.51	99.8714
<i>E. faecalis</i>	<i>P. aeruginosa</i>	2.336	33.6	47.7	91.25	99.8367
<i>E. faecalis</i>	<i>P. fluorescens</i>	2.256	35.9	53	93.42	99.8653
<i>S. pneumoniae</i>	<i>C. subterraneus</i>	2.395	33.2	54.8	92.12	99.8599
<i>S. pneumoniae</i>	<i>P. aeruginosa</i>	2.472	35.7	51.5	93.35	99.8673
<i>S. pneumoniae</i>	<i>P. fluorescens</i>	2.394	36.7	49.9	94.52	99.8791
<i>C. subterraneus</i>	<i>P. aeruginosa</i>	2.723	33.2	51.3	89.86	99.676
<i>C. subterraneus</i>	<i>P. fluorescens</i>	2.607	31.9	51.6	91.56	99.7205
<i>P. aeruginosa</i>	<i>P. fluorescens</i>	0.6	73.4	83.8	98.41	99.9943

^aDynamic similarity values in terms of RMSIP and BC are given in percentages for comparison purposes (RMSIP or BC * 100)

^bAll similarity scores were calculated using only the C- α atoms of Alr homologs

333 Exploring inhibitor binding sites on Alr_{Mtb}

334 Large-scale docking simulations (For details, see Methods) between the lead
335 inhibitors (Fig 1) and the ensemble conformations (of the close-open transition) led to the
336 following conclusions:

337 **Substrate binding cavity is the primary target site of L2-04.** L2-04 penetrated the
338 substrate binding cavity in a majority of Vina and PatchDock complexes (122 Vina
339 complexes; 103 PatchDock complexes (Table S1)). The aromatic ring side of L2-04 was
340 often found in pi-stacking interactions between the inner gate residues, Tyr366 and Tyr273'
341 (residue labeled with a prime to indicate that it belongs to the opposite monomer) while its
342 tail formed hydrogen bonds with the cofactor in the substrate binding cavity of Alr_{Mtb}.
343 Substrate binding cavity measures 5.5 X 5.0 X 2.5 Å³ and accommodates the substrate, L-
344 alanine. Many guest substrates, substrate analogues and inhibitors such as acetate,
345 propanoate, L-alanine phosphonate, lysine and D-cycloserine have been reported to occupy
346 this cavity in homologs [13–15, 17, 44]. In the crystal structure of a thermo-stable Alr of a

347 novel thermophile, *Caldanaerobacter subterraneus subsp. tengcongensis* [21], the substrate
348 is found between the catalytic residues, Lys40 and Tyr268 (equivalent to Lys44 and Tyr273
349 in Alr_{Mtb}) in the substrate binding cavity and forms hydrogen bonds (2.7 Å) with the catalytic
350 tyrosine. We found that the substrate, alanine (Fig S12) and L2-04 docked similarly, into the
351 active site of Alr_{Mtb}, through hydrogen bonds with the hydroxyl 'O' atoms of the catalytic
352 tyrosine, Tyr273' (bond length:2.79 Å) and the cofactor PLP (bond length:2.91 Å). In a few
353 complexes, L2-04 also formed salt bridges with the catalytic lysine (Lys44) of the enzyme. A
354 superposition of the docked Alr—L2-04 complex with the crystal structures of Alr-ligand
355 complexes from *Bacillus anthracis* (Ames), *S. aureus*, *P. fluorescens* and *B.*
356 *stearothermophilus* (Fig 9A) uncovered conserved enzyme residues interacting with the
357 ligands across the complexes. Thus, the network of interactions of L2-04 with the active site
358 residues, especially with the conserved catalytic residues, Lys44, Tyr273 and the cofactor
359 PLP explains the effective abolition of racemization. Our results are in agreement with
360 previous reports [28] which suggest that L2-04 binds Alr_{Mtb} reversibly. We propose that L2-
361 04 brings about reversible, competitive inhibition, where a competition set up between L2-04
362 and the substrate for the same space in the substrate binding cavity induces the establishment
363 of a dynamic equilibrium between the two species. The relative concentrations of the
364 substrate and L2-04, then decide the course of the catalytic process to proceed or terminate
365 intermittently.

Fig 9. Docking of inhibitors to different pockets in Alr_{Mtb}. A. Superposition of the substrate binding cavities of Alr with various bound ligands. Substrate binding cavity residues are shown as sticks and surfaces for reference. Ligands are represented as coloured sticks: docked L2-04 (green sticks); crystallized alanine (pink sticks) in Alr of *C. subterraneus subsp. tengcongensis*, PDB ID: 4Y2W; crystallized propanoate (orange sticks) in Alr of *E. faecalis*, PDB ID: 3E5P; crystallized 4-amino-isoxazolidin-3-one (cyan sticks) in Alr of *G. stearothermophilus*, PDB ID: 1XQL; crystallized acetate (yellow sticks) in Alr of *P. fluorescens*, PDB ID: 2ODO. B. L2-05 docked to active site in the closed state of Alr_{Mtb} (Vina pose 1, Binding affinity: -8.5 kcal/mol; PatchDock poses 1 to 10). Note the entry of L2-05 (yellow sticks) into the 'Second cavity opposite to PLP' (cavity residues depicted as red sticks and surfaces) and the formation of hydrogen bonds (blue lines) with the residues

Lys135, Arg142 in this cavity. Part of the inhibitor is still in substrate binding cavity (cavity residues depicted as green sticks and surfaces). C. L2-13 poses (yellow and orange spheres) docked to putative regulatory pockets in a cartoon representation of the closed form of Alr_{Mtb}. (Orange spheres represent Vina pose 7 / PatchDock pose 7 docked to RS pocket corresponding to monomer B—binding affinity -8.2 kcal/mol; Yellow spheres represent Vina Pose 8 / PatchDock poses 3, 8 docked to RS pocket corresponding to monomer A—binding affinity -8.1 kcal/mol).

366 **The target site extends into a cavity on the opposite side of PLP.** Unexpectedly, a sizeable
367 number of substrate poses bonded with residues of a second, larger ($6.0 \times 4.5 \times 7.5 \text{ \AA}^3$)
368 cavity adjacent to the active site on the opposite side of PLP. This cavity which has been
369 previously characterized in *M. tb* by LeMagueres et al. [12] is accessible from the active site
370 cavity. We refer to this cavity as ‘Second cavity opposite to PLP’ in this study. A very small
371 number of high affinity poses of L2-05, L2-06, L2-10 and L2-13 were found to interact with
372 the residues (Trp90, Lys135, Arg142 and His174) found in this cavity. Regardless of such
373 interactions, none of the inhibitors were capable of occupying this cavity completely due to
374 the presence of two or more ring systems in their bulky structures. Therefore, this cavity is
375 less suitable for accommodating ligands of higher molecular weights, such as L2-05, L2-06,
376 L2-10 and L2-13 (size range=370–470 daltons). Fig 9B shows L2-05 targeting a part of this
377 cavity. Because the poses of all the 4 inhibitors are often found stretched between the active
378 site and the second cavity, we believe that both the cavities are more suitable for ligands of
379 lower molecular weight such as alanine (89 daltons).

380 **Allosteric coupling to close-open movements are mediated by linker residues of a short**
381 **helix.** L2-05, L2-06, L2-10 and L2-13 (Fig 9C) targeted RS pockets multiple times through
382 consensus pocket residues that included arginine, alanine and glycine. A consistent feature in
383 all of the enzyme-inhibitor complexes was the interaction of the inhibitor with the pocket
384 residues, Asp46 and Arg378, both of which were charged and placed adjacent to each other.
385 Asp46 is situated on the same short helix (H2) of the active site TIM-barrel as the catalytic
386 lysine (K44). While Lys44 is present on the inside of the active site TIM-barrel, Asp46 is

387 present on the outside surface of the TIM barrel on the same short helix, but extending into
388 the RS pockets.

389 Superposition of the open and closed states, both of whose RS pockets were
390 bound with high affinity inhibitor poses (Fig 10A), clearly demonstrated the twisted active
391 site cavity in case of the closed state. Docked poses of the bound inhibitors were observed to
392 interact with charged RS pocket residues, Arg378 or Asp46 or both and such interactions
393 appears to be driving the pull experienced by the short helix, H2 (Y48-G47-D46-A45-K44),
394 seen in the normal mode motions. Such a movement of the short helix (Fig 10B) between the
395 active site cavity and the RS pocket leads to the expansion and contraction of the active site
396 cavities, as observed in the conformations of LF₈. The catalytic residue, Lys44, linked by a
397 covalent bond with the cofactor PLP on the inside of the TIM-barrels of the active site cavity
398 (Fig 2C), would be dragged along with Lys44 towards the periphery of the active site cavity.
399 As a result, the orientation of the catalytic residues would be lost. Tyr48, which walls the
400 substrate binding cavity on one side through its side chain, forms the other end of the short
401 helix and therefore would also be displaced, leading to the rearrangement of the substrate
402 binding cavity (Fig 10B). Thus, the dynamic interactions between the inhibitor and the
403 enzyme residues, viz., Arg378---Asp46 (R378---D46), is hypothesized to result in the short
404 helix motion and aid in the communication between the regulatory and the active sites. This
405 communication paradigm adequately explains the basis of signal (inhibitor binding to the
406 regulatory site) transduction from the environment, all the way to the interior of the enzyme
407 active site. The conservation of the charged arginine (Arg378) in the RS pockets across
408 homologs (20 of the 21 homologs) point to a pivotal role for this residue in inhibitor
409 interactions and regulation. In the short helix (YGD_{AK}), the flanking residues, viz. the
410 catalytic Lys44 and the active site residue, Tyr48 are completely conserved while the three
411 middle residues showed equivalent substitutions (Glycine (G) by alanine (18/21), aspartic

412 acid (D) by asparagine (14/21 times), Alanine (A) by either glycine (3/21) or serine (2/21))
413 (Fig 3D). A novel measure for amino acid flexibility in peptides devised by Huang et al. [45]
414 ranks all the three middle residues of the short helix as highly flexible residues in the order,
415 Glycine > Serine > Alanine, Aspartic acid and Asparagine. This result is in agreement with
416 the need for higher conformational flexibility in the short helix residues in order to move
417 between the RS pocket and the active site upon inhibitor binding. Supporting the above
418 results, NMA studies show that deformation energies of the short helix residues are higher
419 than the surrounding structure, indicating higher local flexibility (Fig 7). Generally, in TIM-
420 barrel structures, there is a repetition of 8 alternating α helices and β strands. But, in case of
421 alanine racemases, the arrangement of the active site TIM-barrel is as follows: $\alpha 1$ - $\beta 1$ - $\alpha 2$ - $\alpha 3$ -
422 $\beta 2$ - $\alpha 4$ - $\beta 3$ - $\alpha 5$ - $\beta 4$ - $\alpha 6$ - $\beta 5$ - $\alpha 7$ - $\beta 6$ - $\alpha 8$ - $\beta 7$ - $\alpha 9$ - $\alpha 10$ - $\beta 8$. It appears that the short helix H2 ($\alpha 2$), is an
423 additional insertion (most likely by the splitting of the original second helix into $\alpha 2$ and $\alpha 3$)
424 into the conventional TIM-barrel arrangement, the insertion event evolving probably later, in
425 order to carry out allosteric regulation.

Fig 10. Distortion of active site geometry in mycobacterial Alr. A. Residue positions in the superimposed open and closed states. L2-10 docked to RS pockets in the closed state shown as orange ball and sticks (Vina pose 6 / PatchDock pose 10; Vina binding affinity: -9.1 kcal/mol); L2-10 docked to RS pockets in the open state shown as green ball and sticks (Vina pose 6 / PatchDock pose 5; Vina binding affinity: -8.3 kcal/mol). B. Depiction of the short helix (H2) residue displacements upon the binding of a hypothetical ligand. Tyr48 (Y48 delimits the substrate binding cavity on one side) and Lys44-PLP adduct (K44-PLP adduct important in catalysis) being pulled away from their original positions towards the periphery of active site cavity upon the binding of a representative inhibitor to Asp46, a regulatory pocket residue.

426 The structures of L2-05, L2-06, L2-10 and L2-13 are novel and not analogs
427 of the substrate. Previous mass spectrometric analysis [28] have shown that three (L2-05, L2-
428 06 and L2-13) of these inhibitors bind to the enzyme irreversibly. In these experiments, the
429 binding mode of L2-10 could not be ascertained on account of an ambiguous peak profile.
430 The irreversible binding displayed by the three (L2-05, L2-06 and L2-13) inhibitors in the

431 mass spectrometry experiments when considered together with the docking results showing
 432 RS pocket-bound high affinity inhibitor poses, suggests that allosteric interactions of the
 433 inhibitors with the charged pocket residues (Asp46, Arg378) causes the irreversible inhibition
 434 of the enzyme.

435 **Which of the enzyme states are catalytically active?** In the open state, the inner gates of
 436 the active site entrance were the farthest from each other and were completely open. In
 437 agreement, ensemble docking simulations showed that the substrate docked to the substrate
 438 binding cavity in the open state (Active site 1) and intermediate conformations but not in the
 439 closed state. In the open state, the substrate formed non-covalent interactions with the same
 440 set of conserved active site residues as seen in the crystal structure of the thermo-stable Alr
 441 (PDB ID: 4Y2W of *Caldanaerobacter subterraneus subsp. tengcongensis*) (Table 4). In
 442 contrast, the active site entrance was twisted and closed in the closed state, rendering the
 443 entryway (active site entrance) inaccessible. In such a shut active site cavity, catalysis is not
 444 feasible. Therefore, we reason that the open state is catalytically active.

Table 4 Hydrogen bonds between L-alanine and alanine racemase residues

Structure	Type	Organism	Active site no.	Pose no.	Distance between L-alanine and PLP (Å)	Distance between L-alanine and Tyr273 or equivalent (Å)	Distance between L-alanine and Met321 or equivalent (Å)	Distance between L-alanine and Tyr292 or equivalent (Å)
Crystal structure	Reference structure	<i>Caldanaerobacter subterraneus subsp. tengcongensis</i>	1	-	-	2.67	2.56	2.8
			2	-	2.91	2.96	-	-
State 8 (open state)	Normal mode conformat	<i>Mycobacterium tuberculosis</i>	1	10	2.86, 3.06	-	3.22	-

State 10	ions		1	8	2.84, 3.09	-	3.19	-
State 13			1	8	2.87, 3.03	-	3.12	-
State 18			1	8	2.74	3.03	3.1	-
State 19			2	8	-	3.00	2.89	2.96, 3.04
State 20			2	9	-	2.99	2.94	2.93, 2.98
State 21			2	9	-	2.97	2.99	2.93, 2.95

445 **Conclusion**

446 Despite the increasing popularity of allosteric inhibitors as potential
447 therapeutic agents [46], the structural basis of the mechanism behind allosteric enzyme
448 inhibition remains virtually unknown. Alr_{Mtb} has more than one active site as is characteristic
449 of an allosteric enzyme. The presence of pockets at a location physically distant from the
450 active site together with the fact that the pocket volumes are optimum to house molecules in
451 the size range of natural regulators (activators or inhibitors), reinforces the theory of
452 allostery. The closure of the putative regulatory pockets, occurring as part of native dynamics
453 indicates that such an event is part of the catalytic process. Without the occupation of the
454 pockets by natural modulators during catalysis *in vivo*, it would be needless for the pockets to
455 be undergoing opening and closing movements. Moreover, docking of inhibitors to the
456 putative regulatory pockets, as evidenced by the ensemble docking results, fortify the
457 allostery proposal. Conservation of close-open enzyme movements across several Alr
458 homologs and the presence of 2 distinct states (closed and open RS pockets) in the crystal
459 structures of different organisms make a strong case for a generic allosteric mechanism of
460 regulation in alanine racemases.

461 In conclusion, computational investigations on alanine racemases aided in
462 identifying new, potentially druggable pockets on Alr_{Mtb}, bringing it back into focus as a
463 promising drug target. Many marketed TB drugs are orthosteric ligands and cross-react with
464 eukaryotic PLP-dependent enzymes limiting their usefulness as effective drugs. A
465 pharmacophore model based on the knowledge of scaffolds of the newly identified,
466 potentially druggable pockets will open doors to the discovery of novel, specific, allosteric
467 antimicrobials against *M. tb* with lesser side effects. The normal mode fluctuations between
468 the two different enzyme states is a testable computational hypothesis for experimental
469 studies aimed at deciphering the regulatory mechanism of alanine racemization. Correlation
470 of the short helix (Y48-G47-D46-A45-K44) motion to inhibitor binding at the allosteric site
471 detailed in this work offers a structural basis for allosteric site-to-active site communication
472 in Alr_{Mtb}. Inferences on the nature of inhibitor binding are in good agreement with
473 preliminary mass spectrometric experimental findings by Anthony *et al.* [28]. Mutation
474 studies of the conserved residues of the putative allosteric sites will help in determining the
475 role and essentiality of these new sites in the regulation of catalysis. The presence of
476 conserved residues in the putative regulatory pockets and the similarity in the fluctuation
477 profiles of Alr homologs points to a mode of regulation common to several bacterial species.
478 The disruption of this common regulatory mechanism by targeting the new pockets with a
479 single inhibitor in diverse bacterial pathogens is a prospective tip for the discovery of broad-
480 spectrum antibiotics in future drug discovery efforts.

481 **Methods**

482 **Preparation of *M. tb* alanine racemase structure**

483 The PDB [47] structure of mycobacterial alanine racemase (PDB id: 1XFC)
484 was retrieved and analyzed. Missing internal and terminal residues in each of the monomers

485 (10 N-terminal, 3 C-terminal residues) were constructed on Phyre-2 server [48] and a
486 standalone version of Modeller (v. 9.16) [49]. The revision of sequence information as per
487 the latest release of UniProt-KB [50] (UniProt id: P9WQA9), necessitated the splicing of 2
488 extra residues, 'methionine' and 'alanine' before the N-terminus prior to modelling. Initially,
489 Modeller optimized the model by the variable target function method (VTFM) with conjugate
490 gradients (CG). Subsequently, a preparatory molecular dynamics (MD) procedure with
491 simulated annealing (SA) (300 steps each of heating the model *in vacuo* from 150K to 1300K
492 and 1000 steps each of cooling the structure from 1300K to 300K) and a final, short
493 conjugate gradient optimization (43 steps) were carried out by Modeller. An elaborate energy
494 minimization of the model was additionally carried out by utilizing GROMACS [51] with
495 AMBER-99SB* [52] forcefield on the MDWeb server [53] (500 steps of energy
496 minimization of H atoms followed by 500 steps of energy minimization of the structure
497 restraining heavy atoms to their initial positions with a force constant of 500kj / mol*nm²).
498 The energy minimized model, thus obtained, was assessed on PDBSUM / PROCHECK [54,
499 55] and ERRAT [56] by analyzing Ramachandran plots [57] and other stereo-chemical
500 parameters. Secondary structures of the missing termini were predicted on the PSIPRED v
501 3.3 webserver [58].

502 **Comparative analysis of alanine racemase homologs**

503 A PSI-BLAST v.2.7.0 [59, 60] search for Alr homologs against the PDB
504 database yielded 16 distinct PDB structures in the last iteration (e-value threshold = 0.0001)
505 from 16 different organisms. Out of the 16, 14 were anabolic alanine racemases (Alr) and 2
506 were catabolic alanine racemases (Alr2/DadX). All the 16 sequences were aligned on the
507 ENDscript 2.0 web server [61] using the in-built Clustal Omega tool [62]. Upon examination
508 of the PDB structures of these 16 sequences, eight of them (*M. tuberculosis* (PDB code:

509 1XFC), *S. lavendulae* (PDB code: 1VFH), *E. faecalis* (PDB code: 3E5P), *E. coli* (PDB code:
510 2RJG), *P. aeruginosa* (PDB code: 1RCQ), *P. fluorescens* (PDB code: 2ODO), *S. pneumoniae*
511 (PDB code: 3S46), *C. subterraneus subsp. tengcongensis* (PDB ID: 4Y2W)) were found to be
512 completely resolved and were selected for all further analyses. Root Mean Square Deviation
513 (RMSD) between the aligned C- α coordinates of the atom pairs of the corresponding Alr
514 homologs were calculated in order to compare the similarity of native structures between any
515 two homologs.

516 **All-atom normal mode analysis on individual Alr structures**

517 Elastic network, Tirion-style normal mode models of alanine racemases
518 from *M. tb* (dimer model of PDB id: 1XFC) and 6 completely resolved Alr homologs viz.,
519 those of *Streptomyces lavendulae* (PDB id: 1VFH), *Escherichia coli* (PDB id: 2RJG, 2RJH),
520 *Streptococcus pneumoniae* (PDB id: 3S46), *Enterococcus faecalis* (PDB id: 3E5P, 3E6E),
521 *Pseudomonas aeruginosa* (PDB id: 1RCQ), *Pseudomonas fluorescens* (PDB id: 2ODO) were
522 generated on NOMAD-Ref web server [63] to explore collective, functionally relevant
523 movements in the enzymes. The first 10 non-trivial, low frequency normal modes were
524 generated for all atoms of the enzyme from each microorganism. As there is no provision
525 currently to include cofactors in NMA calculations, PLP was excluded in the NMA
526 calculations and was remodeled later into the NMA ensemble conformations prior to
527 docking.

528 NOMAD-Ref calculates the modes by considering a highly simplified,
529 quadratic potential energy between atoms that are assumed to be linked by a spring of
530 universal strength. The atom-pairs linked by such a spring of an arbitrary elastic constant of
531 $100 \text{ kcal / mol / \AA}^2$, were considered to be located $<10 \text{ \AA}$ away in all the examined PDB
532 structures. Eigen frequencies of the normal modes were generated after weighting all the

533 interactions by $\exp(-(d_{ij}(0)/d_0)^2)$, where d_0 is the distance-weight parameter, which
534 effectively introduced a smoother "cut-off" value than the original Tirion model. Negative
535 eigenvalues were set to zero in the final output [63]. We obtained all our elastic models by
536 applying a distance weight parameter value of 6.8 Å for the elastic constant and utilized the
537 in-built Arnoldi iterative algorithm in order to diagonalize a sparse hessian matrix of $n \times n$
538 dimensions (for example: $n=17238$ in *M. tb*). The amplitude of the protein movement was
539 controlled by fixing the average RMSD at 5 Å in output trajectories.

540 **Comparative normal mode analysis of Alr homologs**

541 In order to study the fluctuations in the conserved regions of the racemases,
542 ensemble-NMA elastic models of the superimposed invariant core of the enzyme across the 8
543 completely resolved Alr and DadX structures discussed before were generated on the eNMA
544 module of a standalone implementation of Bio3D v. 2.1-1 package [64]. In general, for all
545 downstream analyses, the data was filtered and only the first 10 low-frequency modes of each
546 homolog were included in the calculations. In ensemble-NMA calculations, multiple
547 sequence and structural alignment methods are utilized to analyse homologs. From these
548 alignments, equivalent atom positions across structure ensembles were selected and normal
549 mode vectors determined by calculating the effective force constant Hessian matrix K as,

$$550 \quad \hat{K} = K_{AA} - K_{AQ}K_{QQ}^{-1}K_{QA} \quad (1)$$

551 where K_{AA} represents the sub-matrix of K corresponding to the aligned C- α atoms, K_{QQ} for
552 the gapped regions, and K_{AQ} and K_{QA} are the sub-matrices relating the aligned and gapped
553 sites [65]. The normal modes of the individual structure in the ensemble can then be obtained
554 by solving the eigenvalue problem,

$$555 \quad V^T \hat{K} V = \lambda \quad (2)$$

556 where V is the matrix of eigenvectors and λ , the associated eigenvalues.

557 In order to analyze the flexibility profile of the mycobacterial racemase,
558 cross-correlations of residual fluctuations and deformation energy profiles were generated on
559 the filtered normal mode data. Across homologs, the alanine racemase motions along the
560 selected normal modes were compared with the help of similarity measures, viz., RMSIP and
561 Bhattacharyya coefficient.

562 **Flexibility measures to assess Alr_{Mtb}**

563 **Dynamic cross-correlation maps (DCCM)** The correlated motions undergone by C- α atoms
564 of Alr_{Mtb} protein during the first ten low-frequency normal modes were calculated using the
565 Bio-3D DCCM module. The DCCM module generates a covariance matrix between residue
566 pair fluctuations, i, j covering the entire length of the mycobacterial enzyme [66]. A cross-
567 correlation coefficient is then calculated for each residue pair using the equation,

$$568 \quad A_{ij} = \frac{\langle \Delta x_i \Delta y_j \rangle}{\sqrt{\langle \Delta x_i^2 \rangle} \sqrt{\langle \Delta y_j^2 \rangle}} \quad (3)$$

569 Here, Δx_i and Δy_j correspond to the displacement of i^{th} and j^{th} residues from their mean
570 positions.

571 **Deformation energy profiles** Deformation energies were calculated from raw Eigen energies
572 and vectors of the first 10 normal modes of Alr_{Mtb} (NMA based on C- α atoms) with the help
573 of Bio-3D modules. Deformation energy is a normalised measure of the energy contributed
574 by individual atoms of the model towards deformations of the structure [67].

575 **Similarity measures for comparison of enzyme motion across homologs**

576 **Root mean square inner product (RMSIP)** For comparing sets of normal modes, the root
577 mean squared inner product (RMSIP) of the first 10 low frequency modes are generally

578 included [68]. The RMSIP quantifies the similarity of the directions of these low energy
579 subspaces (the subset of low frequency normal modes) between any two given proteins.
580 RMSIP measures the cumulative overlap between all pairs of the ‘l’ largest eigenvectors, and
581 is defined as:

$$582 \quad \text{RMSIP} = \left[\frac{1}{l} \sum_{i=1}^l \sum_{j=1}^l (v_i^A \cdot v_j^B) \right]^{1/2} \quad (4)$$

583 where v_i^A and v_j^B represent the i^{th} and j^{th} eigenvectors obtained from protein A and B,
584 respectively, ‘l’ is the number of modes included (normally 10). The RMSIP measure varies
585 between 0 (orthogonal) and 1 (identical directionality).

586 **Bhattacharyya coefficient** The Bhattacharyya’s coefficient (BC) provides a means to
587 compare two covariance matrices derived from NMA of two given proteins. For ensemble
588 normal modes, the covariance matrix (C) can be calculated as the pseudo inverse of the mode
589 eigenvectors:

$$590 \quad C = \sum_{i=1}^{3N-6} \frac{1}{\lambda_i} v_i v_i^T \quad (5)$$

591 where v_i represents the i^{th} eigenvector, λ_i the corresponding eigenvalue, and N, the number
592 of C- α atoms in the protein structure (3N-6 non-trivial modes). As formulated by Fuglebakk
593 et al. [69], the Bhattacharyya coefficient can then be written as,

$$594 \quad BC = \exp \left[-\frac{1}{2q} \ln \left(\frac{|\Lambda|}{(|Q^T C_A Q| |Q^T C_B Q|)^{1/2}} \right) \right] \quad (6)$$

595 where Q is a matrix in which columns are eigenvectors of the averaged covariance matrix
596 $(C_A + C_B)/2$, Λ is a diagonal matrix containing the corresponding eigenvalues, and q the
597 number of modes needed to capture 90% of the variance (cumulative eigenvalues) of Q. The
598 BC varies between 0 and 1, and equals to 1 if the covariance matrices, C_A and C_B are
599 identical.

600 Docking simulations on the NMA ensemble conformations of Alr_{Mtb}

601 Five potential drug-like inhibitors (Fig 1) from Anthony et al. (2011) [28]
602 were short-listed and subjected to docking simulations against the LF₈ ensemble of Alr_{Mtb}.
603 Prior to ensemble docking, the structures of the small molecules were prepared as elaborated
604 below: 3D structures of the inhibitors were analyzed for all possible tautomers, stereoisomers,
605 and major microspecies at pH 7 on the Chemicalize web server [70]. Lowest energy
606 conformers were generated on a standalone implementation of Chemaxon MarvinView
607 v.16.3.7.0 [71] by applying a Dreiding forcefield [72] at a diversity limit of 0.1 for a time
608 limit of 1000s. L-alanine, the native substrate of the enzyme was included in the ligand set.

609 In an attempt to achieve higher accuracy, we employed AD Vina v.1.1.2
610 [73], which has an advanced scoring function and conducts a more exhaustive sampling of
611 the possible binding modes. To minimize false positives, we applied two other docking
612 algorithms with diverse search methodologies, viz., SwissDock [74] and PatchDock [75] for
613 validation purposes. Although all the 3 docking algorithms employed robust methodologies
614 for searching as well as scoring, we based our analyses primarily on AD Vina results. This
615 strategy was adopted to nullify the bias exhibited by PatchDock and SwissDock towards
616 active site cavities (PatchDock favoured active sites over other locations, while SwissDock
617 clusters seldom entered active sites).

618 In addition to flexible inhibitors, we sought to introduce an implicit
619 flexibility in the enzyme, by utilizing an ensemble of conformations, which sampled relevant
620 functional movements. For this purpose, we selected 15 non-redundant conformations (9th to
621 23rd describing the ‘close-open’ transition) out of the 30 conformations defining the second
622 low frequency mode 8 (LF₈) of *M. tb* Alr, for all analysis. A total of 900 Alr-ligand
623 complexes describing 10 best binding poses for each enzyme-ligand pair resulted from AD

624 Vina runs. These results were validated by checking for identical target sites across 900
625 PatchDock complexes and approximately 3000 SwissDock clusters of binding poses with
626 significant energies.

627 In general, the input structures were prepared according to the specifications
628 of the docking software, retaining default values for all input parameters. In case of AD Vina,
629 exhaustiveness factor was increased proportionally in view of the larger volumes of the
630 search spaces probed, because of which, a minimum of around 100 runs were ensured for
631 each enzyme-ligand combination. A standalone version of AutoDock Tools 1.5.6 [76] was
632 used to prepare receptor and ligand structures in all AD Vina runs. AD Vina searches for
633 ligand poses with the help of an iterated local search global optimizer algorithm and scores
634 the results by an empirical X-score like function incorporating knowledge-based potentials.
635 PatchDock finds docking transformations with good shape complementarity and ranks them
636 based on geometric fit and atomic desolvation. SwissDock employs the EADock dihedral
637 space sampling algorithm and incorporates CHARMM22 [77] forcefield energies by way of a
638 multi objective scoring function using the FACTS solvation model [78]. Interactions of the
639 docked ligands resulting from all of the simulation runs were visualized on PLIP v.1.3.2 [79]
640 and an open-source version of PyMOL v.1.8 [80] (built and compiled from source code
641 downloaded from SourceForge [81]).

642 **Pocket analysis**

643 Normal mode conformations were investigated on the CASTp 3.0 [82] web
644 server for the presence of pockets. Consensus enzyme residues targeted by inhibitors across
645 pockets were gleaned by comparing the ligand-enzyme complexes with LigPlot+ v. 1.4.5
646 [83]. For all other input parameters, default values were retained. In general, custom perl
647 scripts were used for all file processing purposes.

648 **Acknowledgments**

649 We acknowledge the open source efforts in facilitating the distribution of
650 vital molecular visualization tools like PyMOL as a freeware and would like to thank the
651 open source software community and the developers in general.

652 **Author contributions**

653 JJ designed and performed the computations and analysis. SC, TRK
654 provided inputs and supervised, administered the entire project. JJ wrote the original draft of
655 the manuscript while SC, TRK reviewed and revised the MS.

656 **References**

- 657 1. World Health Organization [Internet]. World Health Organization. 2018 [cited 20
658 January 2018]. Available from: <http://www.who.int/en/>
- 659 2. Dheda K, Chang K, Guglielmetti L, Furin J, Schaaf H, Chesov D et al. Clinical
660 management of adults and children with multidrug-resistant and extensively drug-
661 resistant tuberculosis. *Clinical Microbiology and Infection*. 2017; 23(3):131-140.
- 662 3. Kumar V, Patel S, Jain R. New structural classes of antituberculosis agents. *Medicinal*
663 *Research Reviews*. 2017; 38(2):684-740.
- 664 4. Awasthy D, Bharath S, Subbulakshmi V, Sharma U. Alanine racemase mutants of
665 *Mycobacterium tuberculosis* require D-alanine for growth and are defective for
666 survival in macrophages and mice. *Microbiology*. 2011; 158 (2):319–327.
- 667 5. Watanabe A, Yoshimura T, Mikami B, Hayashi H, Kagamiyama H, Esaki N. Reaction
668 mechanism of alanine racemase from *Bacillus stearothermophilus*. *Journal of*
669 *Biological Chemistry*. 2002; 277 (21):19166-19172.

- 670 6. Wild J, Hennig J, Lobočka M, Walczak W, Kłopotowski T. Identification of the dadX
671 gene coding for the predominant isozyme of alanine racemase in *Escherichia coli* K12.
672 MGG Molecular & General Genetics. 1985; 198(2):315-322.
- 673 7. Wasserman SA, Walsh CT, Botstein D. Two alanine racemase genes in *Salmonella*
674 *typhimurium* that differ in structure and function. J Bacteriol. 1983; 153(3):1439-50.
- 675 8. Strych U, Huang H, Krause K, Benedik M. Characterization of the alanine racemases
676 from *Pseudomonas aeruginosa* PAO1. Current Microbiology. 2000; 41(4):290-294.
- 677 9. Strych U, Benedik M. Mutant analysis shows that alanine racemases from
678 *Pseudomonas aeruginosa* and *Escherichia coli* are dimeric. Journal of Bacteriology.
679 2002; 184(15):4321-4325.
- 680 10. Patrick W, Weisner J, Blackburn J. Site-directed mutagenesis of Tyr354 in
681 *Geobacillus stearothermophilus* alanine racemase identifies a role in controlling
682 substrate specificity and a possible role in the evolution of antibiotic resistance.
683 ChemBioChem. 2002; 3(8):789.
- 684 11. Wu D, Hu T, Zhang L, Chen J, Du J, Ding J et al. Residues Asp164 and Glu165 at the
685 substrate entryway function potently in substrate orientation of alanine racemase from
686 *E. coli*: Enzymatic characterization with crystal structure analysis. Protein Science.
687 2008; 17(6):1066–1076.
- 688 12. LeMagueres P, Im H, Ebalunode J, Strych U, Benedik M, Briggs J et al. The 1.9 Å
689 crystal structure of alanine racemase from *Mycobacterium tuberculosis* contains a
690 conserved entryway into the active site. Biochemistry. 2005; 44(5):1471–1481.
- 691 13. Shaw J, Petsko G, Ringe D. Determination of the structure of alanine racemase from
692 *Bacillus stearothermophilus* at 1.9Å resolution. Biochemistry. 1997; 36(6):1329–1342.

- 693 14. Morollo A, Petsko G, Ringe D. Structure of a Michaelis complex analogue:
694 Propionate binds in the substrate carboxylate site of alanine racemase. *Biochemistry*.
695 1999; 38(11):3293-3301.
- 696 15. Stamper G, Morollo A, Ringe D. Reaction of alanine racemase with 1-aminoethyl
697 phosphonic acid forms a stable external aldimine. *Biochemistry*. 1999; 38(20):6714-
698 6714.
- 699 16. Kobayashi J, Yukimoto J, Shimizu Y, Ohmori T, Suzuki H, Doi K et al.
700 Characterization of *Lactobacillus salivarius* alanine racemase: Short-chain
701 carboxylate-activation and the role of A131. *SpringerPlus*. 2015; 4(1):639.
- 702 17. LeMagueres P, Im H, Dvorak A, Strych U, Benedik M, Krause K. Crystal structure at
703 1.45 Å resolution of alanine racemase from a pathogenic bacterium, *Pseudomonas*
704 *aeruginosa*, contains both internal and external aldimine forms. *Biochemistry*. 2003;
705 42(50):14752–14761.
- 706 18. Couñago R, Davlieva M, Strych U, Hill R, Krause K. Biochemical and structural
707 characterization of alanine racemase from *Bacillus anthracis* (*Ames*). *BMC Structural*
708 *Biology*. 2009; 9(1):53.
- 709 19. Scaletti E, Luckner S, Krause K. Structural features and kinetic characterization of
710 alanine racemase from *Staphylococcus aureus* (*Mu50*). *Acta Crystallographica Section*
711 *D Biological Crystallography*. 2011; 68(1):82–92.
- 712 20. Priyadarshi A, Lee E, Sung M, Nam K, Lee W, Kim E et al. Structural insights into the
713 alanine racemase from *Enterococcus faecalis*. *Biochimica et Biophysica Acta (BBA)*
714 — *Proteins and Proteomics*. 2009; 1794(7):1030–1040.
- 715 21. Sun X, He G, Wang X, Xu S, Ju J, Xu X. Crystal structure of a thermostable alanine
716 racemase from *Thermoanaerobacter tengcongensis* MB4 reveals the role of Gln360 in
717 substrate selection. *PLOS ONE*. 2015; 10(7):e0133516.

- 718 22. Im H, Sharpe M, Strych U, Davlieva M, Krause K. The crystal structure of alanine
719 racemase from *Streptococcus pneumoniae*, a target for structure-based drug design.
720 BMC Microbiology. 2011; 11(1):116.
- 721 23. Noda M, Matoba Y, Kumagai T, Sugiyama M. Structural evidence that alanine
722 racemase from a d-cycloserine-producing microorganism exhibits resistance to its own
723 product. Journal of Biological Chemistry. 2004; 279(44):46153-46161.
- 724 24. Sharma V, Wang Y, Liu W. Probing the catalytic charge-relay system in alanine
725 racemase with genetically encoded histidine mimetics. ACS Chemical Biology. 2016;
726 11(12):3305-3309.
- 727 25. Sun S, Toney MD. Evidence for a two-base mechanism involving tyrosine-265 from
728 arginine-219 mutants of alanine racemase. Biochemistry. 1999; 38(13):4058-65.
- 729 26. Ciustea M, Mootien S, Rosato A, Perez O, Cirillo P, Yeung K et al.
730 Thiadiazolidinones: A new class of alanine racemase inhibitors with antimicrobial
731 activity against methicillin-resistant *Staphylococcus aureus*. Biochemical
732 Pharmacology. 2012; 83(3):368-377.
- 733 27. Lee Y, Mootien S, Shoen C, Destefano M, Cirillo P, Asojo O et al. Inhibition of
734 mycobacterial alanine racemase activity and growth by thiadiazolidinones.
735 Biochemical Pharmacology. 2013; 86(2):222-230.
- 736 28. Anthony K, Strych U, Yeung K, Shoen C, Perez O, Krause K et al. New classes of
737 alanine racemase inhibitors identified by high-throughput screening show
738 antimicrobial activity against *Mycobacterium tuberculosis*. PLoS ONE. 2011;
739 6(5):e20374.
- 740 29. Prasad R, Singh A, Srivastava R, Hosmane G, Kushwaha R, Jain A. Frequency of
741 adverse events observed with second-line drugs among patients treated for multidrug-
742 resistant tuberculosis. Indian Journal of Tuberculosis. 2016; 63(2):106-114.

- 743 30. Yao X, Skjærven L, Grant B. Rapid characterization of allosteric networks with
744 ensemble normal mode analysis. *The Journal of Physical Chemistry B*. 2016;
745 120(33):8276-8288.
- 746 31. Miller D, Agard D. Enzyme specificity under dynamic control: A normal mode
747 analysis of α -lytic protease. *Journal of Molecular Biology*. 1999; 286(1):267-278.
- 748 32. Glantz-Gashai Y, Meirson T, Samson A. Normal modes expose active sites in
749 enzymes. *PLOS Computational Biology*. 2016; 12(12):e1005293.
- 750 33. Fuglebakk E, Tiwari S, Reuter N. Comparing the intrinsic dynamics of multiple
751 protein structures using elastic network models. *Biochimica et Biophysica Acta (BBA)*
752 - General Subjects. 2015; 1850(5):911-922.
- 753 34. Kim J, Chang H, Na S. Identification of tail binding effect of kinesin-1 using an elastic
754 network model. *Biomechanics and Modeling in Mechanobiology*. 2015; 14(5):1107-
755 1117.
- 756 35. Kim M, Li W, Shapiro B, Chirikjian G. A Comparison between elastic network
757 interpolation and MD Simulation of 16S ribosomal RNA. *Journal of Biomolecular*
758 *Structure and Dynamics*. 2003; 21(3):395-405.
- 759 36. Kurkcuglu Z, Bakan A, Kocaman D, Bahar I, Doruker P. Coupling between catalytic
760 loop motions and enzyme global dynamics. *PLoS Computational Biology*. 2012;
761 8(9):e1002705.
- 762 37. Hetényi C, van der Spoel D. Blind docking of drug-sized compounds to proteins with
763 up to a thousand residues. *FEBS Letters*. 2006; 580(5):1447-1450.
- 764 38. Hassan N, Alhossary A, Mu Y, Kwoh C. Protein-ligand blind docking using
765 QuickVina-W with inter-process spatio-temporal integration. *Scientific Reports*. 2017;
766 7(1):15451.

- 767 39. Hetényi C, Spoel D. Toward prediction of functional protein pockets using blind
768 docking and pocket search algorithms. *Protein Science*. 2011; 20(5):880-893.
- 769 40. Levy R, Perahia D, Karplus M. Molecular dynamics of an α -helical polypeptide:
770 Temperature dependence and deviation from harmonic behaviour. *Proceedings of the*
771 *National Academy of Sciences*. 1982; 79(4):1346–1350.
- 772 41. Swaminathan S, Ichiye T, Van Gunsteren W, Karplus M. Time dependence of atomic
773 fluctuations in proteins: analysis of local and collective motions in bovine pancreatic
774 trypsin inhibitor. *Biochemistry*. 1982; 21(21):5230–5241.
- 775 42. Tama F, Sanejouand Y. Conformational change of proteins arising from normal mode
776 calculations. *Protein Engineering, Design and Selection*. 2001; 14(1):1–6.
- 777 43. Fuglebakk E, Echave J, Reuter N. Measuring and comparing structural fluctuation
778 patterns in large protein datasets. *Bioinformatics*. 2012; 28(19):2431–2440.
- 779 44. Asojo, O., Nelson, S., Mootien, S., Lee, Y., Rezende, W., Hyman, D., Matsumoto, M.,
780 Reiling, S., Kelleher, A., Ledizet, M., Koski, R. and Anthony, K. (2014). Structural
781 and biochemical analyses of alanine racemase from the multidrug-resistant *Clostridium*
782 *difficile* strain 630. *Acta Crystallographica Section D Biological Crystallography*,
783 70(7), pp.1922-1933.
- 784 45. Huang F, Nau W. A Conformational Flexibility Scale for Amino Acids in Peptides.
785 *Angewandte Chemie International Edition*. 2003; 42(20):2269-2272.
- 786 46. Wenthur C, Gentry P, Mathews T, Lindsley C. Drugs for allosteric sites on receptors.
787 *Annual Review of Pharmacology and Toxicology*. 2014; 54(1):165–184.
- 788 47. Berman HM, Westbrook J, Feng Z, Gilliland G, Bhat TN, Weissig H, et al. The
789 Protein Data Bank. *Nucleic Acids Res*. 2000; 28: 235–242.
- 790 48. Kelley L, Mezulis S, Yates C, Wass M, Sternberg M. The Phyre2 web portal for
791 protein modeling, prediction and analysis. *Nature Protocols*. 2015; 10(6):845–858.

- 792 49. Webb B, Sali A. Comparative protein structure modeling using MODELLER. Current
793 Protocols in Protein Science. 2016 Nov 1; 86:2.9.1–2.9.37.
- 794 50. The UniProt Consortium. UniProt: the universal protein knowledgebase. Nucleic Acids
795 Research. 2017; 45 (D1):D158–D169.
- 796 51. Abraham M, Murtola T, Schulz R, Páll S, Smith J, Hess B et al. GROMACS: High
797 performance molecular simulations through multi-level parallelism from laptops to
798 supercomputers. SoftwareX. 2015; 1–2:19–25.
- 799 52. Lindorff-Larsen K, Piana S, Palmo K, Maragakis P, Klepeis J, Dror R et al. Improved
800 side-chain torsion potentials for the Amber ff99SB protein force field. Proteins:
801 Structure, Function, and Bioinformatics. 2010; 78(8):1950–8.
- 802 53. Hospital A, Andrio P, Fenollosa C, Cicin-Sain D, Orozco M, Gelpí J. MDWeb and
803 MDMoby: an integrated web-based platform for molecular dynamics simulations.
804 Bioinformatics. 2012; 28(9):1278–1279.
- 805 54. de Beer T, Berka K, Thornton J, Laskowski R. PDBsum additions. Nucleic Acids
806 Research. 2013; 42(D1):D292–D296.
- 807 55. Laskowski R, MacArthur M, Moss D, Thornton J. PROCHECK: a program to check
808 the stereochemical quality of protein structures. Journal of Applied Crystallography.
809 1993; 26(2):283–291.
- 810 56. Colovos C, Yeates T. Verification of protein structures: Patterns of non-bonded atomic
811 interactions. Protein Science. 1993; 2(9):1511–1519.
- 812 57. Ramachandran G, Ramakrishnan C, Sasisekharan V. Stereochemistry of polypeptide
813 chain configurations. Journal of Molecular Biology. 1963; 7(1):95–99.
- 814 58. Buchan D, Minneci F, Nugent T, Bryson K, Jones D. Scalable web services for the
815 PSIPRED protein analysis workbench. Nucleic Acids Research. 2013; 41(W1):W349–
816 W357.

- 817 59. Altschul S. Gapped BLAST and PSI-BLAST: a new generation of protein database
818 search programs. *Nucleic Acids Research*. 1997; 25(17):3389–3402.
- 819 60. Schaffer A. Improving the accuracy of PSI-BLAST protein database searches with
820 composition-based statistics and other refinements. *Nucleic Acids Research*. 2001;
821 29(14):2994–3005.
- 822 61. Robert X, Gouet P. Deciphering key features in protein structures with the new
823 ENDscript server. *Nucleic Acids Research*. 2014; 42(W1):W320–W324.
- 824 62. Sievers F, Wilm A, Dineen D, Gibson T, Karplus K, Li W et al. Fast, scalable
825 generation of high-quality protein multiple sequence alignments using Clustal Omega.
826 *Molecular Systems Biology*. 2014; 7(1):539–539.
- 827 63. Lindahl E, Azuara C, Koehl P, Delarue M. NOMAD-Ref: visualization, deformation
828 and refinement of macromolecular structures based on all-atom normal mode analysis.
829 *Nucleic Acids Research*. 2006; 34(Web Server):W52–W56.
- 830 64. Grant B, Rodrigues A, ElSawy K, McCammon J, Caves L. Bio3d: an R package for
831 the comparative analysis of protein structures. *Bioinformatics*. 2006; 22(21):2695–
832 2696.
- 833 65. Skjærven L, Yao X, Scarabelli G, Grant B. Integrating protein structural dynamics and
834 evolutionary analysis with Bio3D. *BMC Bioinformatics*. 2014; 15(1):399.
- 835 66. Ichiye T, Karplus M. Collective motions in proteins: A covariance analysis of atomic
836 fluctuations in molecular dynamics and normal mode simulations. *Proteins: Structure,
837 Function, and Genetics*. 1991; 11(3):205–217.
- 838 67. Hinsen K. Analysis of domain motions by approximate normal mode calculations.
839 *Proteins: Structure, Function, and Genetics*. 1998; 33(3):417–429.
- 840 68. Amadei A, Ceruso M, Di Nola A. On the convergence of the conformational
841 coordinates basis set obtained by the essential dynamics analysis of proteins' molecular

- 842 dynamics simulations. *Proteins: Structure, Function, and Genetics*. 1999; 36(4):419–
843 424.
- 844 69. Fuglebakk E, Reuter N, Hinsen K. Evaluation of protein elastic network models based
845 on an analysis of collective motions. *Journal of Chemical Theory and Computation*.
846 2013; 9(12):5618–5628.
- 847 70. Chemicalize—Instant Cheminformatics Solutions [Internet]. Chemicalize.com. 2018
848 [cited 21 January 2018]. Available from: <https://chemicalize.com>
- 849 71. ChemAxon—Software Solutions and Services for Chemistry & Biology [Internet].
850 Chemaxon.com. 2018 [cited 21 January 2018]. Available from:
851 <http://www.chemaxon.com>
- 852 72. Mayo S, Olafson B, Goddard W. DREIDING: a generic force field for molecular
853 simulations. *The Journal of Physical Chemistry*. 1990; 94(26):8897–8909.
- 854 73. Trott O, Olson A. AutoDock Vina: Improving the speed and accuracy of docking with
855 a new scoring function, efficient optimization, and multithreading. *Journal of*
856 *Computational Chemistry*. 2009; 31(2):455–61.
- 857 74. Grosdidier A, Zoete V, Michielin O. SwissDock, a protein-small molecule docking
858 web service based on EADock DSS. *Nucleic Acids Research*. 2011; 39(suppl):W270–
859 W277.
- 860 75. Schneidman-Duhovny D, Inbar Y, Nussinov R, Wolfson H. PatchDock and
861 SymmDock: servers for rigid and symmetric docking. *Nucleic Acids Research*. 2005;
862 33(Web Server):W363–W367.
- 863 76. Morris G, Huey R, Lindstrom W, Sanner M, Belew R, Goodsell D et al. AutoDock4
864 and AutoDockTools4: Automated docking with selective receptor flexibility. *Journal*
865 *of Computational Chemistry*. 2009; 30(16):2785–2791.

- 866 77. Brooks B, Brooks C, Mackerell A, Nilsson L, Petrella R, Roux B et al. CHARMM:
867 The biomolecular simulation program. *Journal of Computational Chemistry*. 2009;
868 30(10):1545–1614.
- 869 78. Haberthür U, Caflisch A. FACTS: Fast analytical continuum treatment of solvation.
870 *Journal of Computational Chemistry*. 2008; 29(5):701–715.
- 871 79. Salentin S, Schreiber S, Haupt V, Adasme M, Schroeder M. PLIP: fully automated
872 protein–ligand interaction profiler. *Nucleic Acids Research*. 2015; 43(W1):W443–
873 W447.
- 874 80. Delano W. The PyMOL molecular graphics system. Open source version 1.3.
875 Schrödinger, LLC; 2011.
- 876 81. PyMOL Molecular Graphics System — Browse /pymol at SourceForge.net [Internet].
877 Sourceforge.net. 2018 [cited 21 January 2018]. Available from:
878 <https://sourceforge.net/projects/pymol/files/pymol/>
- 879 82. Dundas J, Ouyang Z, Tseng J, Binkowski A, Turpaz Y, Liang J. CASTp: computed
880 atlas of surface topography of proteins with structural and topographical mapping of
881 functionally annotated residues. *Nucleic Acids Research*. 2006; 34(Web
882 Server):W116–W118.
- 883 83. Laskowski R, Swindells M. LigPlot+: Multiple ligand–protein interaction diagrams for
884 drug discovery. *Journal of Chemical Information and Modeling*. 2011; 51(10):2778–
885 2786.

886 **Supporting Information**

Figure S1. Multiple sequence alignment of Alr homologs from different bacterial species.

Figure S2. Sequence conservation profile of Alr_{Mtb}.

Figure S3. Dendrogram based on the identity of protein sequences of alanine racemases.

Figure S4. A. Scatter plot of the normal-mode derived fluctuations of conserved residues of

the superimposed homologs. This residue set corresponds to the invariant core of Alr_{Mtb}. B. Scatter plot of the normal-mode derived fluctuations of similar, structurally equivalent residues of the superimposed homologs. All calculations were performed using C- α coordinates of the superimposed invariant core of alanine racemase homologs on the ensemble NMA (eNMA) Bio-3D module.

Figure S5. Dynamic cross-correlation map of residual fluctuations of alanine racemase of *Streptomyces lavendulae*.

Figure S6. Dynamic cross-correlation map of residual fluctuations of alanine racemase of *Enterococcus faecalis*.

Figure S7. Dynamic cross-correlation map of residual fluctuations of alanine racemase of *Streptococcus pneumoniae*.

Figure S8. Dynamic cross-correlation map of residual fluctuations of alanine racemase of *Caldanaerobacter subterraneus subsp. tengcongensis*.

Figure S9. Dynamic cross-correlation map of residual fluctuations of alanine racemase of *Pseudomonas aeruginosa*.

Figure S10. Dynamic cross-correlation map of residual fluctuations of alanine racemase of *Pseudomonas fluorescens*.

Figure S11. Dynamic cross-correlation map of residual fluctuations of alanine racemase of *Escherichia coli*.

Figure S12. LigPlot comparison of the docked substrate pose (L-alanine) of Alr_{Mtb} with homologous Alr complexes co-crystallized with alanine in *Caldanaerobacter subterraneus subsp. tengcongensis*.

Table S1. Results of docking simulation runs of substrate and inhibitors on the ensemble conformations of alanine racemase from *Mycobacterium tuberculosis*.

Table S2. Properties of pockets of NMA ensemble conformations as calculated on the CASTp server.

Text S1. Multiple sequence alignment of Alr homologs utilized in ensemble NMA (shown with alignment positions).

Movie S1. Secondary structure representation of normal mode number 8 in Alr_{Mtb}. N-terminal putative lid-like region is shown in red colour. Helices H3 (yellow) and H4 (violet) undergo displacements.

Figure 1

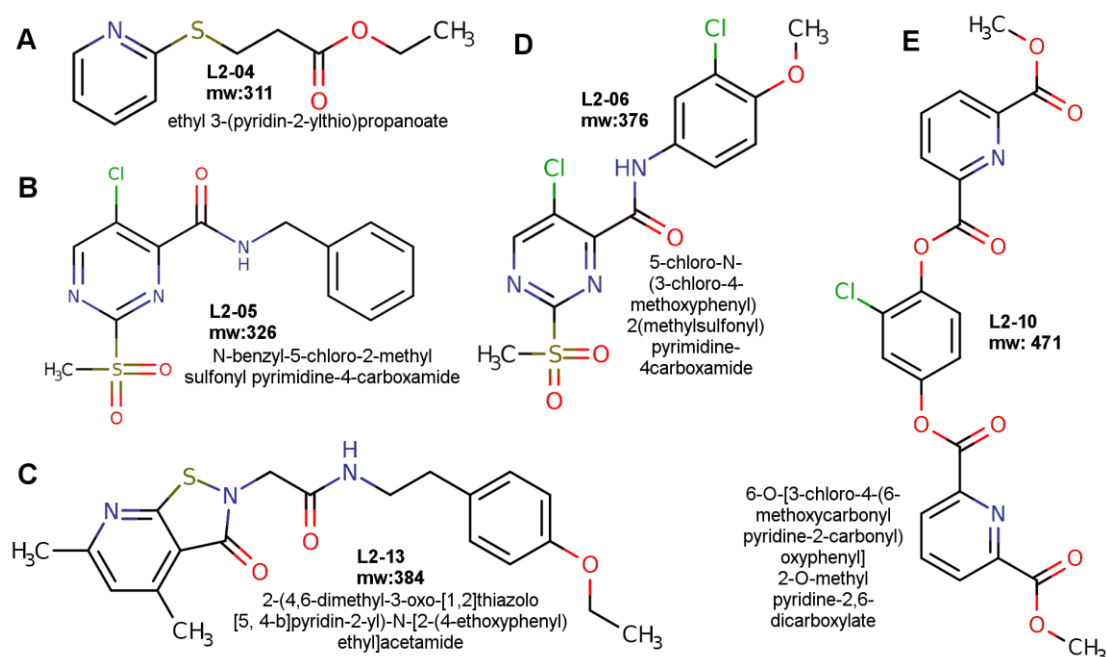


Figure 2

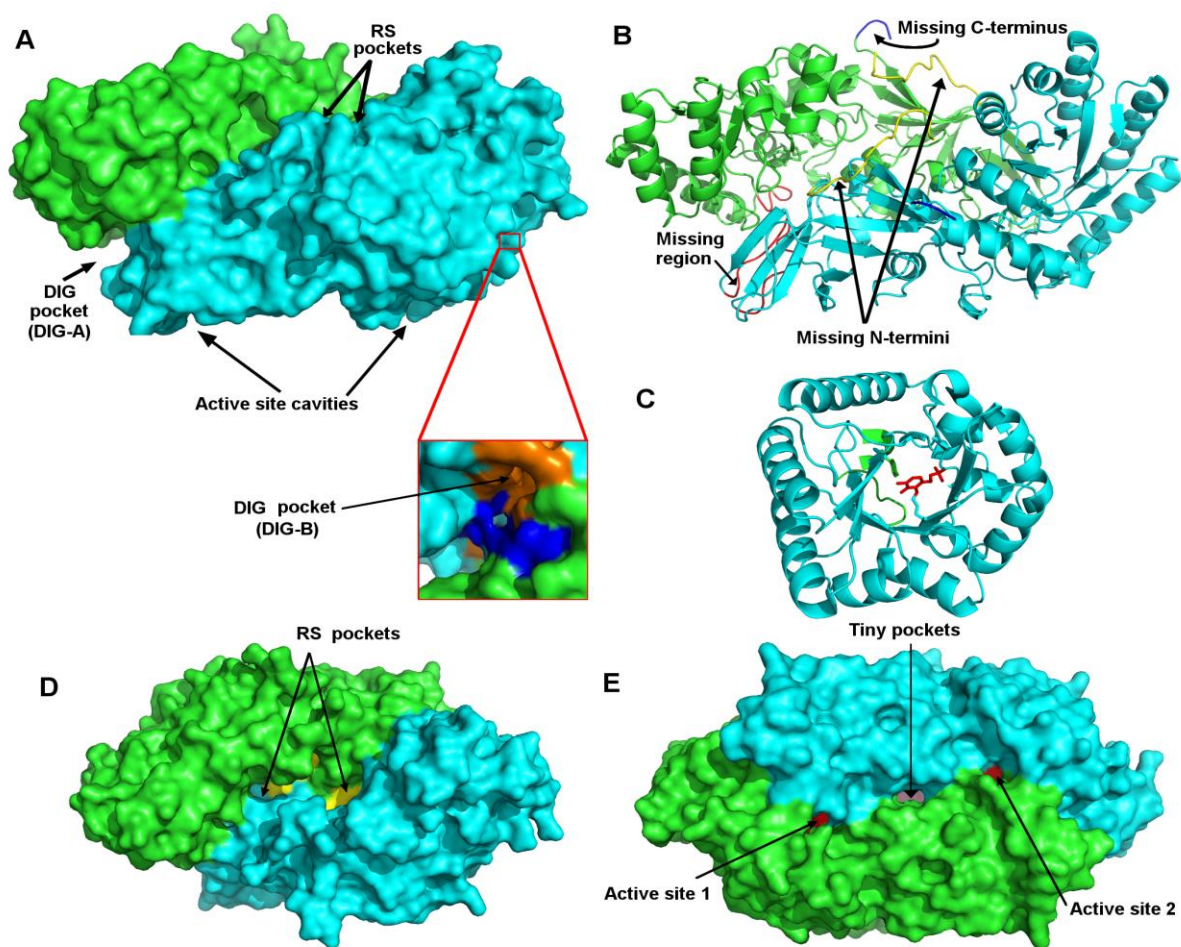


Figure 3

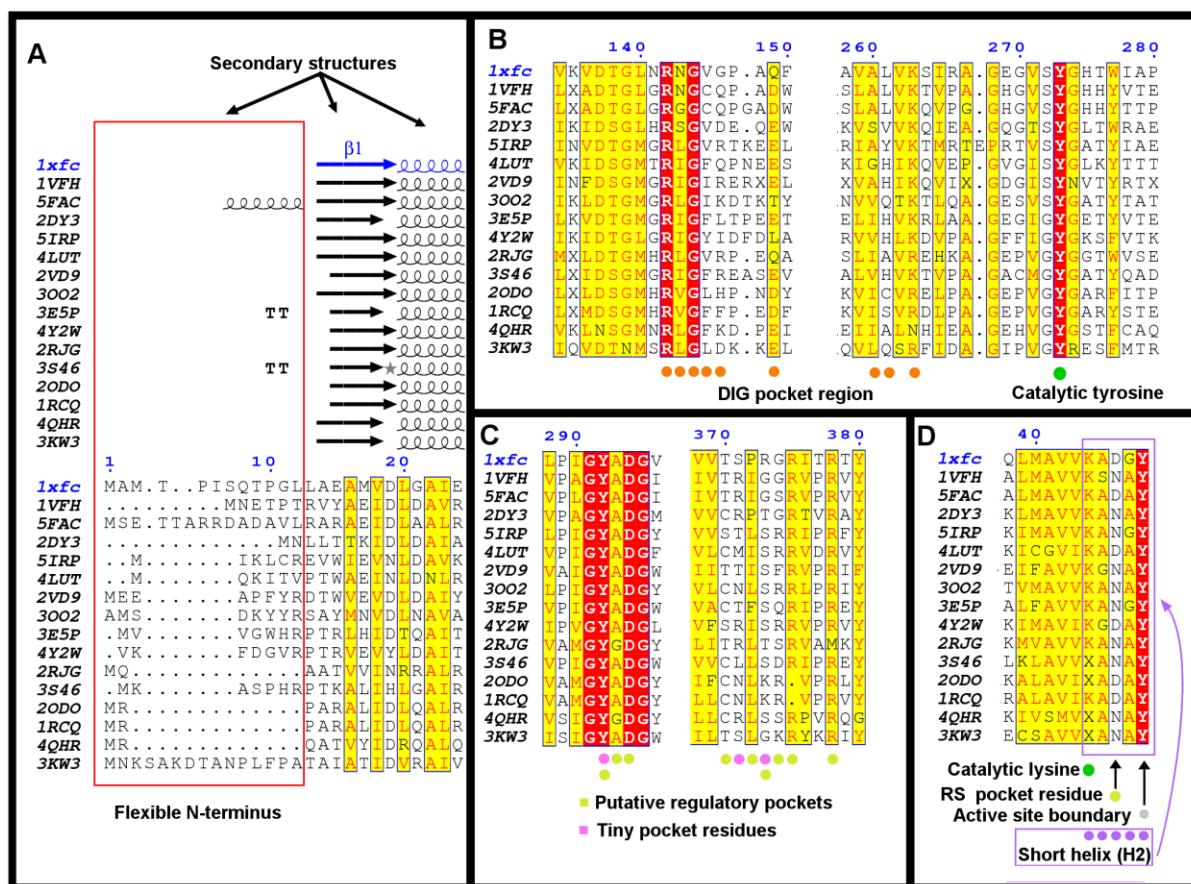


Figure 4

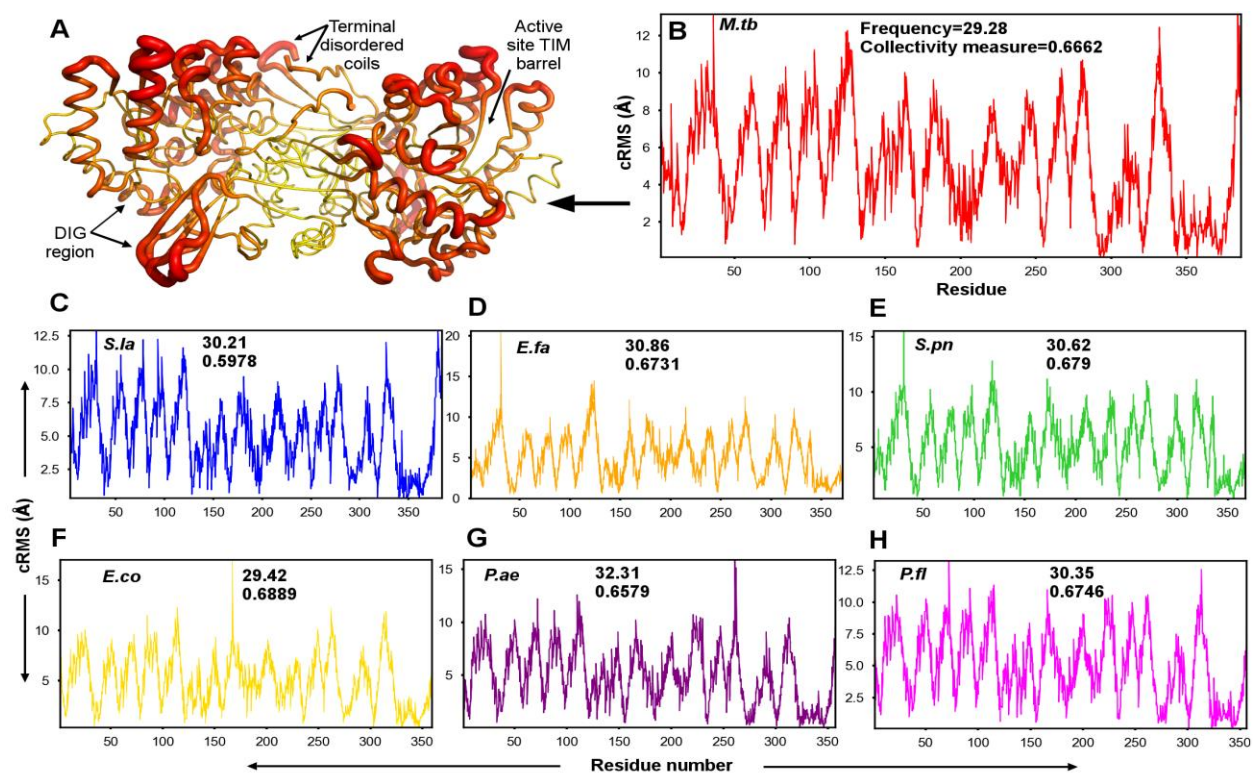


Figure 5

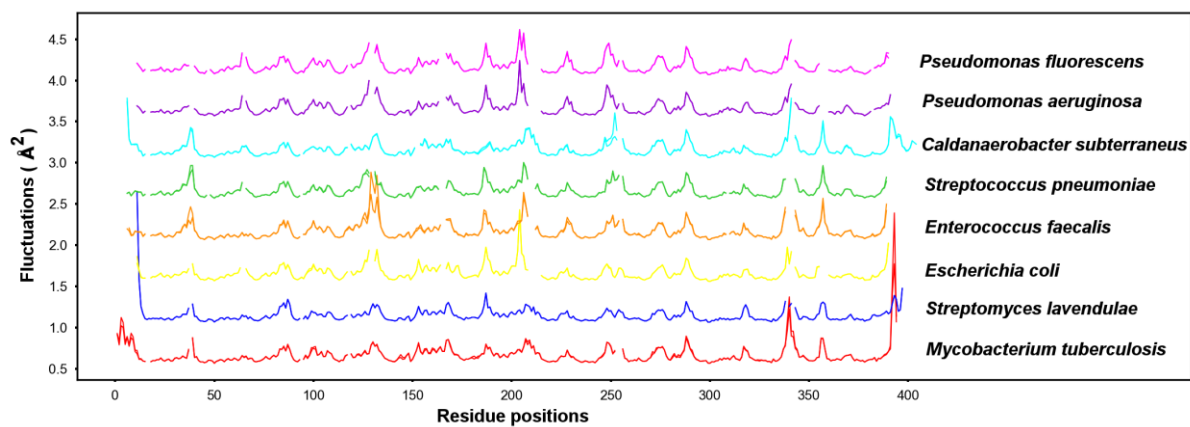


Figure 6

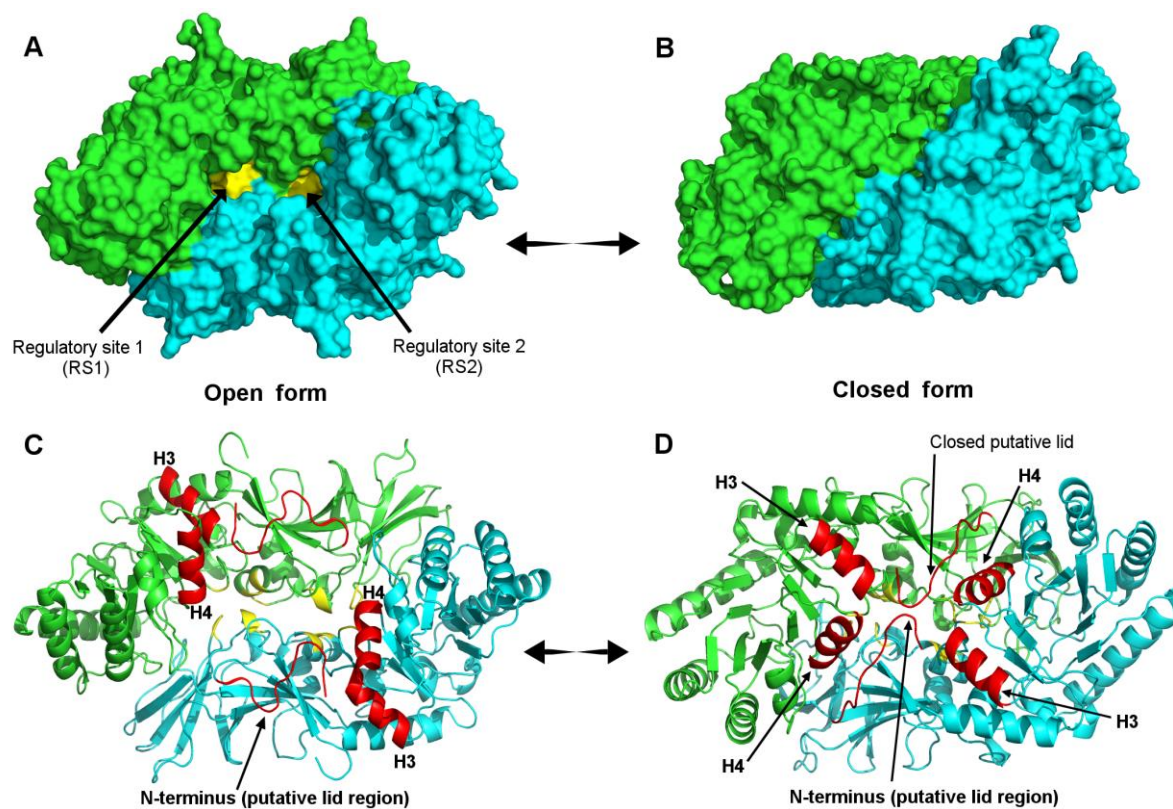


Figure 7

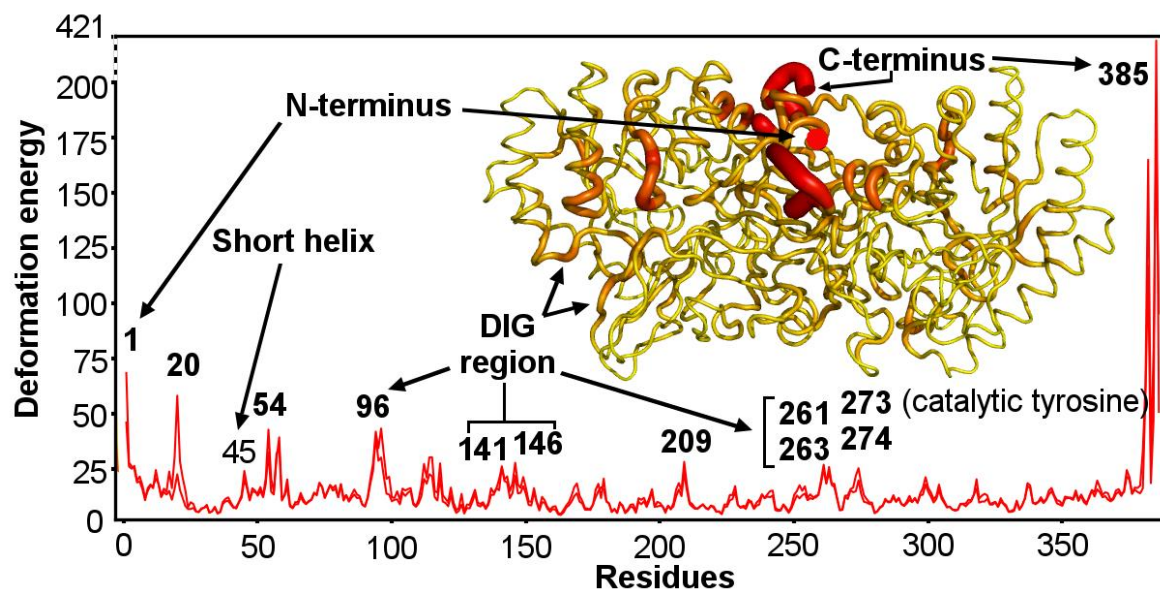


Figure 8

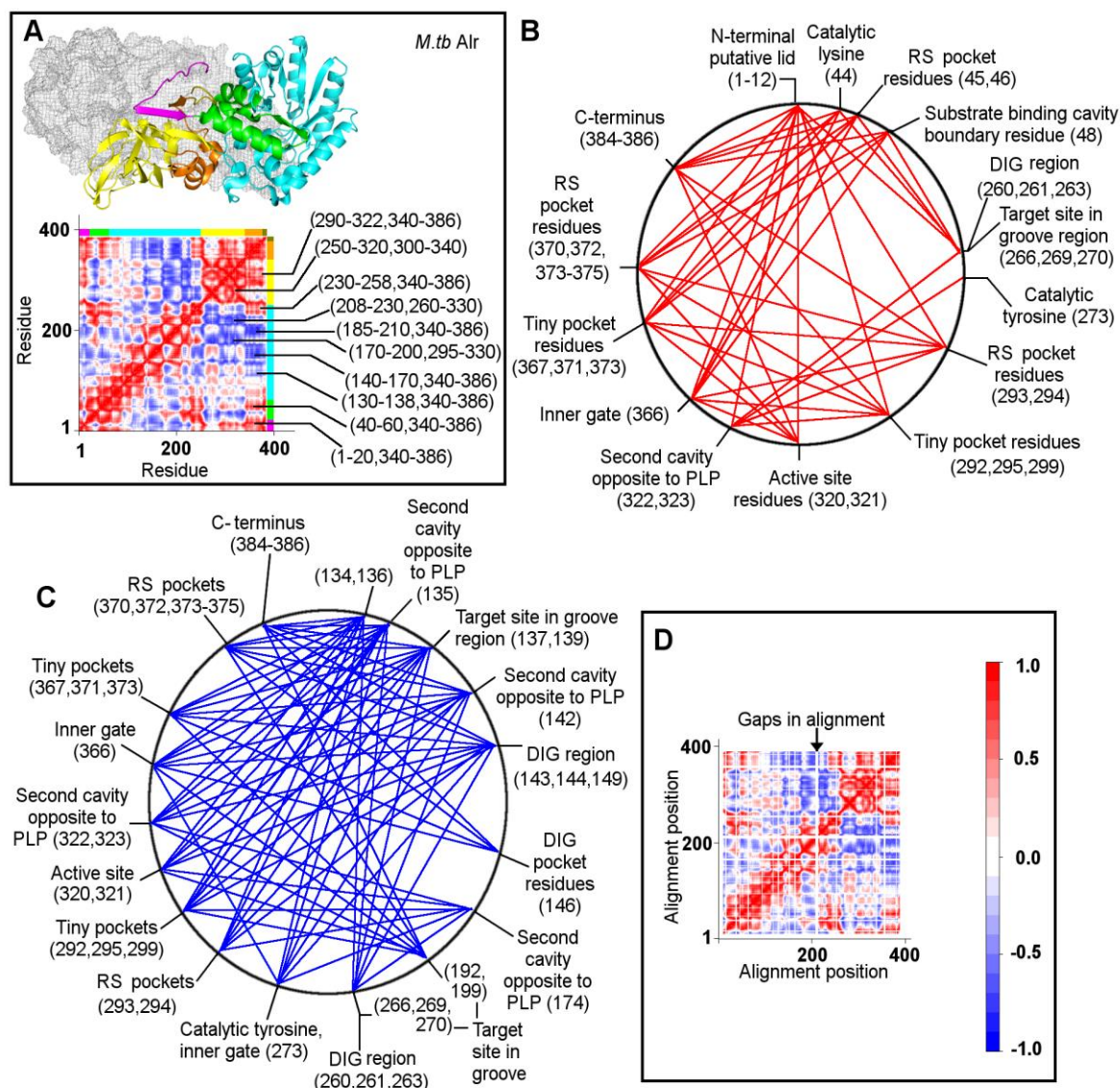


Figure 9

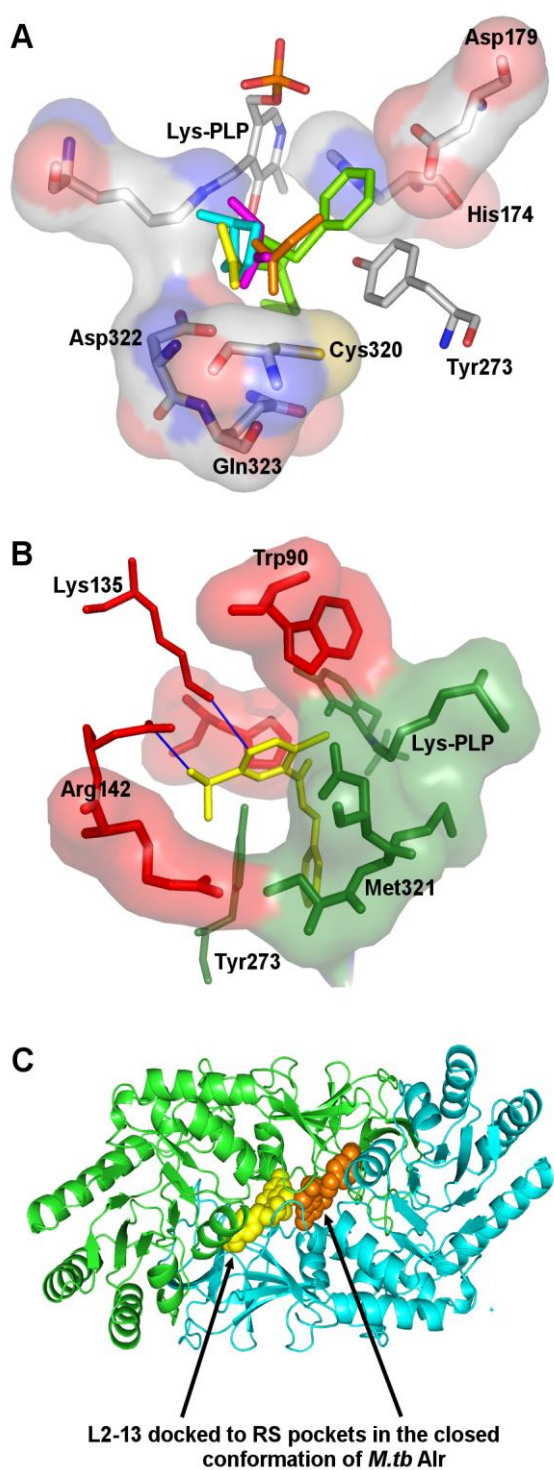


Figure 10

